Geochimica et Cosmochimica Acta 338 (2022) 278–301

Contents lists available at ScienceDirect

Geochimica et Cosmochimica Acta

journal homepage: www.elsevier.com/locate/gca

The case for the angrite parent body as the archetypal first-generation planetesimal: Large, reduced and Mg-enriched

François L.H. Tissot [a,b,*], Max Collinet [a,c], Olivier Namur [d,e], Timothy L. Grove [a]

[a] Department of the Earth, Atmospheric and Planetary Sciences, Massachusetts Institute of Technology, 77 Massachusetts Avenue, Cambridge, MA 02139, USA
[b] The Isotoparium, Division of Geological and Planetary Sciences, California Institute of Technology, Pasadena, CA 91125, USA
[c] Institute of Planetary Research, German Aerospace Center (DLR), Rutherfordstaße 2, 12489 Berlin, Germany
[d] Institute of Mineralogy, Leibniz University Hannover, Callinstrasse 3, 30167 Hannover, Germany
[e] Department of Earth and Environmental Sciences, KU Leuven, Celestijnenlaan 200e, 3001 Heverlee, Belgium

ARTICLE INFO

Article history:
Received 18 June 2022
Accepted 23 September 2022
Available online 7 October 2022
Associate editor: Audrey Bouvier

Keywords:
Angrites
Oxygen fugacity
Piston cylinder
Planetesimal
Planetary building blocks

ABSTRACT

Angrites are silica-undersaturated achondrites formed very early in the history of the Solar System, and the most volatile-depleted known meteorites. As such, the study of angrites can provide critical insights into the early stages of planetary formation, melting and differentiation. Yet, understanding the origins of angrites and the nature of their parent body has long been hindered by the initially small number of specimens available. Here, we leverage (i) the rapidly growing number of known angrites, and (ii) equilibrium crystallization experiments at various pressure, temperature and oxygen fugacity conditions (P-T-fO_2), to revisit the petrogenesis of angrites and constrain key features of the angrite parent body (APB), such as its composition and size.

We observe that quenched (*i.e.*, volcanic) angrites define two compositional groups, which we show are readily related by fractional crystallization. This crystallization trend converges on an olivine-clinopyroxene-plagioclase (Ol + Cpx + Plag) multiple saturation boundary, whose composition is sampled by D'Orbigny, Sahara 99555 and NWA 1296. Using the observation that some quenched specimens represent primitive angritic melts, we derive a self-consistent bulk composition for the APB. We find that this composition matches the proposed Mg/Si ratio of 1.3 derived from the angrite δ^{30}Si values, and yields a core size (18 ± 6 wt%) in agreement with the siderophile elements depletion in the APB mantle. Our results support a primary control of nebular fractionation (*i.e.*, partial condensation) on the composition of the APB. To establish the liquid phase equilibria of angrites, a series of 1 atmosphere and high-pressure crystallization experiments (piston cylinder and internally heated pressure vessel) were performed on a synthetic powder of D'Orbigny. The results suggest that the APB was a large (possibly Moon-sized) body, formed from materials condensed at relatively high-temperature (~1300–1400 K), and whose fO_2 changed from mildly reducing (~IW-1.5) to relatively oxidizing (~IW+1 ± 1) in the ~ 3 Myr between its core formation and the crystallization of D'Orbigny-like (Group 2) angrites. Based on its timing of accretion and differentiation, its composition, redox, and size, we argue that the APB represents the archetype of the first-generation of refractory-enriched planetesimals and embryos formed in the *innermost* part of the inner Solar System (<1 AU), and which accreted in the telluric planets.

1. Introduction

Named after the type specimen that fell in 1869 in the bay of Angra dos Reis (Brazil), angrites are a series of differentiated meteorites (achondrites) of basaltic composition, which owing to their ancient and pristine nature, have become key samples in the study of the Early Solar System. Indeed, angrites display minimal post-crystallization alteration, metamorphism, shock or impact brecciation (*e.g.*, Keil, 2012 and references therein), and the quenched specimens are some of the earliest known volcanic rocks, with crystallization ages only ~ 4 Myr after the formation of Calcium, Aluminum-rich inclusions (CAIs, the oldest known solids in the Solar System) (*e.g.*, Tissot et al., 2017 and references therein). Furthermore, the angrite parent body (APB) itself is thought to have accreted within the first ~ 0.5–1 Myr of the Solar System

* Corresponding author.
E-mail address: tissot@caltech.edu (F.L.H. Tissot).

https://doi.org/10.1016/j.gca.2022.09.031
0016-7037/

(*e.g.*, Kleine et al., 2012). As such, angrites both act as key anchors for Early Solar System chronology and provide critical insights into the early stages of planetary formation, melting, and differentiation.

For a long time, the limited number of angrite specimens hindered our ability to understand the details of their petrogenesis and the characteristics of the APB. For instance, the seminal work of Longhi (1999) used all of the 4 specimens then available, which included two very similar fine-grained, rapidly-cooled volcanic (*i.e.*, quenched) angrites (Asuka 881371, LEW 87051), one plutonic angrite (LEW 86010) and the very atypical plutonic angrite Angra dos Reis (hereafter, AdoR), a 98 % pyroxene cumulate. Although D'Orbigny had been discovered in 1979, it was not recognized as a meteorite until 1999 (see Keil, 2012), the same year that Sahara 99555 was discovered. These two new meteorites, both quenched in texture, formed the first set of compositionally identical angrites, and seemed to have crystallized from a parental magma similar to that of the previously known two quenched angrites. Yet no simple petrogenetic sequence seemed to be able to explain the entire angrite suite, and multiple source magmas were posited to explain the plutonic LEW 86010 and AdoR (Mittlefehldt et al., 2002; Floss et al., 2003).

Over the last two decades, new meteorite finds, predominantly in the hot deserts of Northern Africa, have steadily increased the size of the angrite suite. Today, this collection counts 37 angrite specimens representing 24 different angrites (Table 1) and including 7 plutonic angrites (AdoR, LEW 86010, NWA 2999, NWA 4590, NWA 4801, NWA 5379, NWA 14758 and their paired specimens), 10 volcanic/quenched angrites (Asuka 12209, Asuka 881371, D'Orbigny, LEW 87051, NWA 1296, NWA 1670, NWA 7203, NWA 7812, NWA 12774 and Sahara 99555), 5 diabasic angrites (NWA 12004, NWA 12320, NWA 12879, NWA 12934 and NWA 13363), 1 dunitic angrite (NWA 8535) and 1 angrite that might represent an intermediate stage between volcanic and plutonic angrites (NWA 10463 and paired specimens, Santos et al., 2016). While numerous studies (mainly conference abstracts) have reported detailed mineralogical, petrological and geochemical characterization for each of these new specimens (*e.g.*, Jambon et al., 2005, 2008; Gellissen et al., 2007; Shirai et al., 2009a; Baghdadi et al., 2013, 2015; Irving et al., 2013, 2019,2020; Santos et al., 2016; Shearer et al., 2016), comparatively little effort has been dedicated to understanding the angrite suite as a whole, and the constraints this augmented family of meteorite places on the nature of the APB (Mikouchi et al., 2004; Riches et al., 2012; McKibbin and O'Neill, 2018; Sanborn and Wadhwa, 2021).

In this paper, we first examine the relationships between angrites, which reveals the existence of two groups of quenched angrites. We show that these two groups are readily related by a fractional crystallization trend, which converges on an olivine-clinopyroxene-plagioclase (Ol + Cpx + Plag) multiple saturation boundary whose composition is sampled by D'Orbigny, Sahara 99555 and NWA 1296. Leveraging the recognition that the least differentiated quenched angrites represent primitive angritic melts, we place novel constraints on the APB's bulk composition, and show that it is primarily controlled by nebular fractionation processes (*i.e.*, partial condensation) rather parent body processing. Through a series of equilibrium crystallization experiments of a synthetic D'Orbigny composition at various pressure, temperature and oxygen fugacity conditions (P-T-fO_2), we then establish the liquid phase equilibria of angrites. These results provide novel constraints on the size and fO_2 of the APB, confirming its reduced nature, while also indicating that the size of the APB has historically been significantly underestimated. Based on these results, we argue that the APB represents the archetype of an important group of early formed, refractory-enriched, planetesimals from which the terrestrial planets accreted.

Table 1
List of all known angrites, as of August 2022.

Sample	Date of find/fall	Location	Mass (g)
Plutonic angrites			
Angra dos Reis	Jan 1869 (Fall)	Bay of Angra dos Reis, Brazil	~1500
LEW 86010	1986	Lewis Cliff, Antarctica	6.9
NWA 2999	2004, 2005	Morocco or Algeria, purchased in Tagounite	392, 2400
*NWA 3158**	2004	NW Africa, purchased in Tagounite	681
*NWA 3164**	2004	Morocco or Algeria, purchased in Rabat	928
*NWA 4569**	2005	NW Africa, purchased in Erfoud	484
*NWA 4662**	2006	NW Africa, purchased in Erfoud	60
*NWA 4877**	2007	NW Africa, purchased in Erfoud	1000
*NWA 4931**	2007	NW Africa, purchased in Tagounite	2140
*NWA 5167**	2007	Morocco, purchased in Erfoud	859
*NWA 6291**	2010	NW Africa, purchased in Morocco	250
*NWA 6705**	2011	NW Africa, purchased in Erfoud	1003
*NWA 10754**	2015	NW Africa, purchased in Paris	770
*NWA 12822**	2019	NW Africa, purchased in Morocco	172
NWA 4590	2006	Morocco/Algeria, purchased in Tagounite	212.8
NWA 4801	2007	Algeria, purchased in Erfoud	252
*NWA 8405**	2014	NW Africa, purchased in Erfoud	501
NWA 5379	2019	NW Africa, purchased in Erfoud	6.1
NWA 14758	2019	NW Africa, purchased in Guelmin	125.5
Intermediate angrites (contain both zoned olivines and olivine with exsolution lamellae)			
NWA 10463	2015	NW Africa, purchased in Erfoud	202.5
*NWA 10646**	2016	NW Africa, purchased in Morocco	14
Quenched angrites			
Asuka 12209	2012	Antarctica	43.65
Asuka 881371	1988	Antarctica	11.3
D'Orbigny	July 1979	Argentina (farm field)	16550
LEW 87051	1987	Lewis Cliff, Antarctica	0.6
NWA 1296	Spring, 2001	Morocco, purchased in Bouarfa	810
NWA 1670	2003	NW Africa, purchased in Morocco	29
NWA 7203	2011	Morocco, purchased in Tucson (Arizona)	107
NWA 7812	2013	NW Africa, purchased in Erfoud	46.2
NWA 12774	2019	NW Africa, purchased in Mauritania	454
Sahara 99555	1999	Sahara	2710
Diabasic angrites			
NWA 12004	2018	Near Touignin, Morocco	183
NWA 12320	2018	Mauritania, purchased in Nouakchott	1946, 2379
NWA 12879	2019	NW Africa, purchased in Morocco	11
NWA 12934	2018	NW Africa	563
NWA 13363	2020	Algeria	54
Dunitic angrite			
NWA 8535	2014	NW Africa, purchased in Guelmin	149

Data source: Keil (2012), Meteoritical Bullletin Database.
* paired to the previous specimen

2. Composition of angrites and previous experimental works

When the compositions (Table 2) of the full suite of known angrites are projected in pseudoquaternary Ol-Cpx-Plag-Qtz diagrams, two groups appear amongst quenched angrites (Fig. 1). Group 1 contains angrites Asuka 881371, LEW 87051, NWA 1670, NWA 5167, NWA 7812 and NWA 12774. It is somewhat diffuse, with ~ 10–15 % compositional variability in any given mineral component between specimens. In contrast, Group 2 is a tightly clustered set of three angrites – D'Orbigny, Sahara 99555 and NWA 1296 – whose compositions are nearly identical. Quenched angrite NWA 7203 plots close to the Group 2 specimens in the Ol-Cpx-Plag projection but not in the Ol-Cpx-Qtz projection, due to its more silica-undersaturated nature. The two diabasic specimens for which bulk compositions have been reported

Table 2
Compilation of bulk composition of angrites (wt%). When multiple estimates available, preferred values in bold font.

Sample	Mass (mg)	SiO_2	TiO_2	Al_2O_3	Fe_2O_3	Cr_2O_3	FeO	MnO	MgO	CaO	Na_2O	P_2O_5	K_2O	NiO	S	Total	Mg#	Ref.
Plutonic angrites																		
AdoR	~660	44.71	2.09	9.26		0.22	10.5	0.12	11.8	23.0	0.03		<0.01	<0.01		101.7	66.5	[1]
AdoR	< 57	43.7	2.05	9.35		0.21	9.4	0.10	10.8	22.9		0.13		0.01		98.7	67.2	[2]
AdoR		43.22	2.33	8.92	2.05	0.20	8.67	0.13	10.54	23.66	0.06	0.09	<0.02	0.03	0.53	100.52	64.1	[3]
AdoR avg		**43.88**	**2.16**	**9.18**	**2.05**	**0.21**	**9.54**	**0.12**	**11.04**	**23.17**	**0.04**	**0.11**	**<0.02**	**0.02**	**0.53**	**102.04**	**63.3**	**[1–3]**
LEW 86010	190	39.6	1.57	14.0		0.13	20.3	0.22	7.30	17.5	0.03		0.04	<0.01		100.7	39.0	**[1]**
LEW 86010	~900	39.6	1.15	14.1		0.11	18.5	0.20	7.0	17.5		0.13				98.3	40.3	[2]
LEW 86010		40.32	1.10	14.09		0.12	18.24	0.20	7.14	18.20		0.21			0.40	100.02	41.1	[4]
LEW 86010		43.3	0.42	12.1		0.37	15.9	0.30	9.4	15.2	<0.01		<0.01			96.99	51.3	[5]
LEW 86010		43	0.9	12		0.23	18	0.2	8.7	18						101.03	46.3	[6]
LEW 86010 avg		**39.83**	**1.27**	**14.06**		**0.12**	**19.02**	**0.21**	**7.15**	**17.73**	**0.03**	**0.17**	**0.04**	**<0.01**	**0.40**	**100.03**	**40.1**	**[1–2,4]**
NWA 2999	120	**33.4**	**0.42**	**4.71**		**0.36**	**31.2**	**0.24**	**19.0**	**7.37**		**<0.1**		**0.59**		**97.30**	**52.1**	[7]
NWA 2999	20–40	(35.4)	0.53	7.0		0.31	29.8	0.21	16.0	10.1				0.67		(100)	48.9	[8]
NWA 2999		37.67	0.23	3.34		0.12	23.46	0.12	21.10	8.58		0.03				94.64	61.6	[9]
NWA 3164[+]	100	(39.32)	0.57	8.35		0.29	22.73	0.26	18.28	9.86	0.01	0.09	0.04			(100)	58.9	[10]
NWA 3164[+]	450	35.37	0.52	7.58		0.26	29.29	0.24	16.60	8.95	0.01	0.08	0.04	0.56		99.50	50.3	[11]
NWA 3164[+*]		38.91	0.51	8.62		0.30	21.21	0.10	19.13	10.87				0.02		99.66	61.7	[11]
NWA 4931[+]	20–40	(31.6)	0.44	10.55		0.37	26.7	0.24	20.7	9.05				0.32		(100)	58.0	[8]
NWA 5167[+]	500	34.68	0.49	10.30		0.31	26.52	0.21	15.12	11.55	0.01	0.02	0.01	0.29		99.50	50.4	[11]
NWA 5167[+*]		39.79	0.51	11.58		0.29	17.79	0.22	16.44	12.6				0.02		99.24	62.2	[11]
NWA 4590		37.49	1.46	8.50		0.09	27.16	0.31	6.80	17.84	0.11	0.18	0.18	<0.01	0.18	100.30	30.9	[12]
NWA 4590		38.25	0.31	10.56		0.10	16.59	0.12	6.19	21.32		0.12				93.55	39.9	[9]
NWA 4801		42.08	1.51	13.75		0.12	10.92	0.11	11.15	19.45		0.12				99.20	64.5	[9]
Intermediate angrites																		
NWA 10463	20–40	(38.6)	1.17	11.0		0.16	24.1	0.26	8.19	16.5				0.02		(100)	37.7	[8]
Quenched angrites																		
Asuka 881371	700	37.30	0.88	10.07	0.63	0.13	23.43	0.20	14.81	12.51	0.03	0.17	0.02	0.03	0.59	100.80	52.4	[3]
D'Orbigny	120	36.9	0.85	12.3		0.05	24.9	0.25	6.45	15.2		0.17				97.07	31.6	[7]
D'Orbigny	20–40	(42.2)	0.77	14.3		0.04	21.1	0.22	5.96	15.4				0.003		(100)	33.5	[8]
D'Orbigny	25/200[**]	38.4	0.89	12.4		0.0419	24.7	0.28	6.49	15.0	0.0172	0.16		0.01		98.39	31.9	[13]
D'Orbigny avg		**37.65**	**0.87**	**12.35**		**0.044**	**24.80**	**0.265**	**6.47**	**15.10**	**0.0172**	**0.17**		**0.01**		**97.74**	**31.7**	**[7,13]**
LEW 87051	27	41.1		10.8		0.16	21.1	0.24	14.9	12.0	0.03		<0.03	<0.01		100.3	55.8	[1]
LEW 87051	22	40.4	0.73	9.19		0.17	19.0	0.24	19.4	10.8		0.08				100.0	64.5	[2]
LEW 87051		38.9	0.6	11.3		0.1	22.1	0.3	13.1	12.7	<0.1	0.1				99.6	51.4	[14]
LEW 87051 avg		**40.12**	**0.67**	**10.42**		**0.144**	**20.73**	**0.261**	**15.81**	**11.85**	**0.03**	**0.09**	**<0.03**	**<0.01**		**100.12**	**57.6**	**[1–2,14]**
NWA 1296	20–40	(36.2)	0.87	14.3		0.08	25.2	0.29	7.25	15.8				0.002		(100)	33.9	[8]
NWA 1296	500	**(39)**	**0.93**	**12.18**		**0.068**	**25.00**	**0.28**	**6.71**	**14.65**	**0.028**	**0.17**	**<0.03**			**(100)**	**32.4**	**[15]**
NWA 1670	500	(42.18)	0.67	11.70		0.14	18.52	0.22	14.60	11.95	0.01	0.12	0.03			(100.14)	58.4	[16]
NWA 7203	20–40	(34.2)	0.99	14.7		0.07	25.4	0.28	7.34	17.1				0.003		(100)	34.0	[8]
NWA 7812		(34.07)	0.54	9.18		0.22	22.04	0.24	18.09	10.03	0.07	0.13	0.01			94.62	59.4	[17]
NWA 12774		39.38	0.59	10.86			20.63	0.23	17.25	10.90	0.32	0.17				100.33	59.8	[18]
S. 99555	120	38.6	0.88	12.9		0.04	25.6	0.27	6.79	15.4		0.18				100.62	32.1	[7]
S. 99555	20–40	(39.0)	0.93	12.3		0.04	25.2	0.27	6.43	15.8				0.007		(100)	31.3	[8]
S. 99555	20–40	(42.7)	0.90	10.8		0.04	24.9	0.27	6.06	14.3				0.006		(100)	30.2	[8]
S. 99555	~200	38.6	0.91	12.5		0.0463	23.1	0.26	7.04	15.1	0.0164	0.15		<0.01		97.72	35.2	[13]
S. 99555 avg		**38.60**	**0.895**	**12.70**		**0.0426**	**24.35**	**0.265**	**6.92**	**15.25**	**0.0164**	**0.165**		**<0.01**		**99.20**	**33.6**	**[7,13]**
Diabasic angrites																		
NWA 12004		(40.1)	0.89	11.74		0.05	24.89	0.27	6.32	14.96	0.03	0.18	0.01		0.43	(100)	31.2	[19]
NWA 12320		(40.4)	0.81	11.83		0.05	24.27	0.26	6.65	15.15	0.02	0.17	0.01		0.42	(100)	32.8	[19]

References: [1] Warren & Kallemeyn (1990), INAA. [2] Mittlefehldt & Lindstrom (1990), fused bead-electron microprobe analysis. [3] Yanai (1994), wet chemical analysis. [4] McKay et al. (1988c), calculated from mode and mineral compositions. [5] Prinz et al. (1988), calculated from mode and mineral compositions. [6] Delaney & Sutton (1988), calculated from mode and mineral compositions. [7] Gellissen et al. (2007), XRF analyses, quoting Wolff PhD thesis for Sah 99555. [8] Zhu et al. (2019) MC-ICPMS, SiO_2 by difference. [9] Sanborn, PhD Thesis (2012), calculated from mode and mineral compositions. [10] Baghdadi et al. (2013), ICP-AES, SiO_2 by difference. [11] Baghdadi et al. (2015), ICP-AES. [12] Shirai et al. (2009a), from analysis of the fusion crust. [13] Mittlefehldt et al. (2002), fused bead-electron microprobe analysis. [14] McKay et al. (1990), calculated from mode and mineral compositions. [15] Jambon et al. (2005), ICP-AES, SiO_2 by difference. [16] Jambon et al. (2008), ICP-AES, SiO_2 by difference. [17] Irving et al. (2013), XRF and ICPMS on wire-saw cutting dust, SiO_2 by difference. [18] Irving et al. (2020), ICP-OES of clean bulk cutting dust. [19] Irving et al. (2019), XRF and ICPMS on wire-saw cutting dust, SiO_2 by difference.

[*] Denotes composition where extraneous metal has been subtracted (see Baghdadi et al. (2015) for details).

[**] Powder split (numerator) from an homogenized mass (denominator).

[+] paired to the previous specimen

(NWA 12004 and NWA 12320) plot tightly with the Group 2 angrites suggesting they formed by the same process.

The invariant position of the Group 2 specimen compositions in the Ol-Cpx-Plag diagram, and their small spread in the Ol-Cpx-Qtz diagram is similar to the systematic observed during fractional crystallization of mid-ocean ridge basalts (MORBs) (Grove et al., 1992). In fact, the quenched Group 2 specimens plot near the Ol-Cpx-Plag-melt saturation boundary calculated at 1 atm for a D'Orbigny-like melt (Mg # 0.32, NaK # = 0, and TiO_2 = 0.9 wt%) (Fig. 1). These observations, along with the presence and textural relationships of Ol, Cpx and Plag in quenched Group 2 angrites (*e.g.*, Floss et al., 2003), suggest that these specimens might have crystallized in shallow magma chamber(s) in equilibrium with Ol-Cpx-Plag, before being erupted and cooled in subsurface conditions. Group 1 angrites, on the other hand, plot in the olivine primary phase space, and could therefore represent samples of a more primitive magma from which the Group 2 specimens were later derived. While too few angrites were available at the time

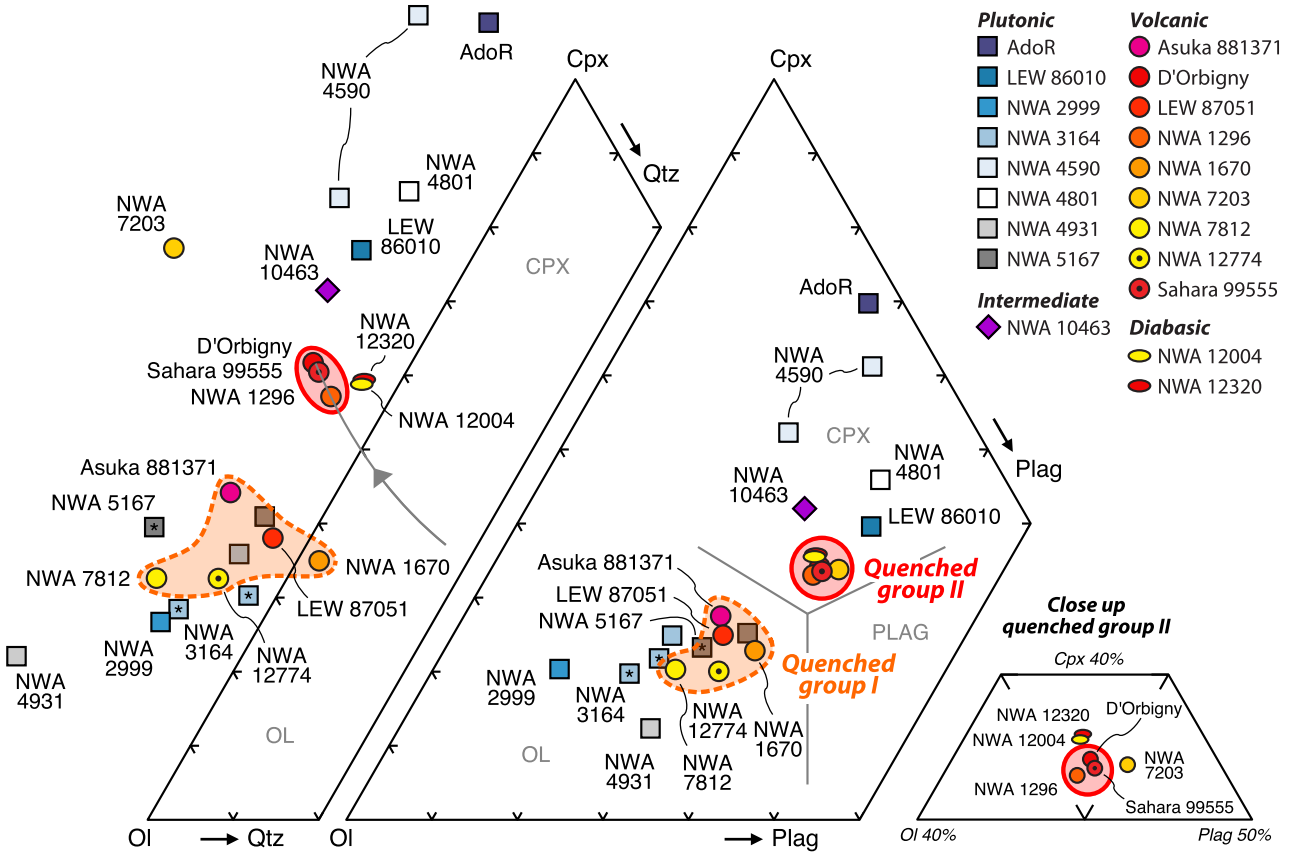

Fig. 1. Pseudoternary Ol-Cpx-Qtz (left) and Ol-Cpx-Plag (center and right) projections showing the bulk composition of angrites. Warm colors are for volcanic angrites, and cold colors for plutonic angrites. The illustrative saturation boundaries are calculated at 1 atm, for a D'Orbigny-like melt (Mg # 0.32, NaK # = 0, and TiO_2 = 0.9 wt%) using the MORB model from Grove et al. (1992). The goal of this work is to establish the actual position of these boundaries and the P-T-fO_2 conditions relevant to the angrites. Note that for NWA 3164/5167, symbols with and without a star denote, respectively, the composition before and after subtraction of extraneous metal (see Baghdadi et al. (2015) for details).

to reveal such a clear systematic between Group 1 and Group 2 quenched angrites, previous work, using major and minor element abundance trends in Ol, Cpx and Plag minerals and cooling rates experiments (Mikouchi et al., 2000, 2004; Floss et al., 2003; Sanborn and Wadhwa, 2010) have proposed an evolutionary relationship between some Group 1 (Asuka 881371, LEW 87051 and/or NWA 1670) and Group 2 specimens (Sahara 99555, D'Orbigny and/or NWA 1296). In Section 5.1, we will show that fractional crystallization from Group 1 liquids converges on the composition of the quenched Group 2 specimens, at the expected Ol-Cpx-Plag saturation boundary.

Equilibration of a given liquid composition with multiple phases only occurs at restricted fO_2-P-T conditions, often indicative of the melting conditions of a particular mineral assemblage (*i.e.*, mantle source) or the conditions at which a liquid stalled in a magma chamber or multi-phase crystal mush (Wyllie et al., 1981). The primary goal of this work is thus to investigate the phase equilibrium of a natural angrite from the quenched Group 2 to place novel constraints on the P-T-fO_2 conditions relevant to the APB early in its magmatic evolution. To date, most angrite experimental studies have aimed to (i) produce angritic melt by partial melting of chondrites (*e.g.*, Allende CV3, Murchison CM2, St. Severin LL, Lost City H, Jurewicz et al., 1991, 1993, 1995, 2004), (ii) determine the trace element equilibrium partition coefficients relevant to silicate minerals in plutonic angrites (McKay et al., 1988a, 1994; Fittipaldo et al., 2005), or (iii) constrain the cooling rates of the quenched angrites via crystallization experiments (Mikouchi et al., 2000, 2001). An early attempt to constraint the phase equilibrium of angrite using synthetic compositions of the plutonic LEW 86010 specimen was done by McKay et al. (1988b), but the authors concluded that their experiments failed to achieve complete equilibrium thus strongly limiting their usefulness. Using liquid boundaries and solid solution parameterizations in the CMAS + Fe system (from Shi, 1992), Longhi (1999) performed a theoretical investigation but was limited by the small number (four) of specimens known then. More recently, McKibbin and O'Neill (2018) reported a series of 1 atm reversal crystallization experiments using synthetic D'Orbigny and Sahara 99555 compositions under both reduced (1.2 log unit below the iron-wüstite buffer: IW-1.2) and oxidized conditions (IW+2.0), to investigate the role of spinel as a sink of Al in the angrite source region and potential cause of the elevated Ca/Al ratios in angritic melts.

Here, we will demonstrate that the more magnesian quenched angrites (Group 1), represent more primitive melts and that the quenched Group 2 angrites are more evolved lavas (Section 5.1), whose invariant position in the pseudo-ternary Ol-Cpx-Plag diagram is due to multiple saturation of their source magma. Because the position of the saturation boundary, as well as the nature of the saturating phases depend on the P-T-fO_2 conditions (*e.g.*, Ol + Cpx + Plag at 1 atm vs Ol + Cpx + Sp above 5–6 kbar), we used equilibrium crystallization experiments to determine the specific P-T-fO_2 relevant to formation of quenched Group 2 angrites. We performed both 1 atm and high-pressure (up to 13 kbar) experiments, under various temperature (from 1106 to 1295 °C)

and oxygen fugacity conditions (from the Iron-Quartz-Fayalite (IQF; ~IW-0.6) buffer to the Quartz-Fayalite-Magnetite (QFM; ~IW+3.6) buffer).

3. Experimental methods

3.1. Synthetic powder preparation

A synthetic powder of D'Orbigny composition (Table 3) was prepared from high-purity oxide powders (Specpure), following the methods of Grove and Bence (1977). To avoid issues arising from hydration of some oxide powders (P_2O_5, CaO, Na_2O, K_2O, FeO), phosphorus was added as $Ca_5(PO_4)_3F$, calcium as $CaSiO_3$, nickel as NiO, and iron as a mixture of Fe and Fe_2O_3. Sodium and potassium were not added given their extremely low abundance in quenched Group 2 angrites. All oxides except NiO and Fe were initially mixed together in a clean agate mortar, covered with ethanol and ground in an automatic grinder for 4 hr. Iron and nickel were then added to the oxide mix and ground for another 40 min. The ethanol + oxide mixture was left to evaporate under a gentle flow of compressed air until dried. The powder was then scraped from the surface of the mortar using weighing paper, and further ground by hand in ethanol with an agate pestle for another 30 min to ensure full homogenization, and dried again.

Using polyvinyl alcohol (Elvanol®), the dried powder was made into a cohesive paste, shaped into small pellets using a clean metal cylinder and rod, and dried under a heat lamp for 1 hr. Dried pellets were suspended using Pt wires in a 1 atm Deltech VT-31 gas mixing furnace, and conditioned for 3 days at 1050 °C at the QFM buffer to react the oxides to more stable minerals. After conditioning, the pellets were finally ground in ethanol in a clean agate mortar and the powder was dried under a heat lamp.

3.2. One atmosphere experiments

A first set of 11 experiments were conducted in the MIT experimental petrology laboratory using a 1 atm Deltech VT-31 vertical furnace to determine the stable mineral assemblage at low-pressure at the liquidus (Table 4). As angrites are thought to have formed under reducing conditions, around the IW buffer (Brett et al., 1977; Mckay et al., 1994; Shearer et al., 2016; Steenstra et al., 2017), five initial experiments were carried out in iron capsules in evacuated silica tubes (Grove and Bence, 1977). Inside the vacuum of the evacuated tube, the combination of Fe (from the capsule) and FeO + SiO_2 (from the sample) maintains the fO_2

Table 3
Major element composition of D'Orbigny (*i.e.*, quenched Group 2) and the synthetic powder used in this work.

	SiO_2	TiO_2	Al_2O_3	Cr_2O_3	FeO	MnO	MgO	CaO	Na_2O	K_2O	P_2O_5	NiO	Total
Average*	37.65	0.87	12.35	0.044	24.80	0.265	6.47	15.10	0.0172		0.165	0.0116	97.74
Normalized	38.52	0.89	12.64	0.045	25.37	0.27	6.62	15.45	0.0176	0	0.169	0.0118	100.00
Synthetic powder	38.49	0.89	12.63	0.036	25.45	0.27	6.61	15.45	0	0	0.160	0.0145	100.00

*Average from this study (see Table 2).

Table 4
Summary of experimental run conditions, results and mass balance calculations.

Run	P	T	Charge[a]	fO_2 buffer	Log fO_2		Dur.[b]	Crystal.	Phases						FeO
		(°C)		Target	Target	Exp.	(hrs)		liq	ol	cpx	plag	sp	Other	loss(-)/gain(+)
Dorb-3	1 atm	1173	Fe	IQF (IW-0.57)	−12.85		73.0	17 %	83.5	6.8		9.9	*		+3.5 %
Dorb-1	1 atm	1153	Fe	IQF (IW-0.59)	−13.14		67.0	27 %	72.5	12.0		15.8	*		+3.3 %
Dorb-2	1 atm	1133	Fe	IQF (IW-0.61)	−13.43		94.5	38 %	62.4	16.9		20.6		Ca-Ol*	+2.7 %
Dorb-4	1 atm	1113	Fe	IQF (IW-0.63)	−13.73		120.3	46 %	53.6	21.6		24.2			+3.6 %
Dorb-11	1 atm	1094	Fe	IQF (IW-0.65)	−14.03		115.5	68 %	32.0	29.6	13.5	24.4			+0.01 %
Dorb-9	1 atm	1136	30–35 % Fe-Pt	IW+0.5	−12.28	−12.18 (IW+0.60)	114.8	32 %	68.3	11.2		16.5			−3.8 %
Dorb-10	1 atm	1120	30–35 % Fe-Pt	IW+0.5	−12.51	−12.29 (IW+0.72)	120.6	53 %	46.6	20.2	10.8	22.0			−0.4 %
Dorb-8	1 atm	1106	30–35 % Fe-Pt	IW+0.5	−12.71	−12.72 (IW+0.49)	137.5	74 %	26.4	28.9	18.3	25.8			−0.1 %
Dorb-6	1 atm	1163	13–25 % Fe-Pt	QFM (IW+3.56)	−8.86	−8.92 (IW+3.50)	46.3	8 %	91.9	1.0		5.7	*		−1.5 %
Dorb-7[c]	1 atm	1151	13–25 % Fe-Pt	QFM (IW+3.57)	−9.00	−8.89 (IW+3.69)	>68.5	N/A	*liq, ol, cpx, plag, sp (magnetite)*						N/A
Dorb-5[d]	1 atm	1132	13–25 % Fe-Pt	QFM (IW+3.59)	−9.25	−9.08 (IW+3.76)	183.3	48 %	52.2	7.8	17.1	17.4	7.1		−0.1 %
IHPV-1	3 kbar	1160	IHPV	CCO (IW+1.81)	−10.53		48	16 %	83.8	8.3		8.4			−0.3 %
IHPV-2	5 kbar	1190	IHPV	CCO (IW+1.88)	−9.99		48	5 %	94.8	3.8			1.0	Fe metal	−2.4 %
B1412	5 kbar	1170	C	IW+1.14	−10.99		28.9	29 %	70.8	11.8	3.8	12.7			−0.3 %
IHPV-3[e]	5 kbar	1170	IHPV	CCO (IW+1.94)	−10.19		48	81 %	18.8	6.4	40.7	21.2		Fe metal	−12.3 %
IHPV-4[e]	5 kbar	1170	IHPV	CCO (IW+1.94)	−10.19		48	63 %	37.4	6.0	34.4	12.4	0.8	Fe metal	−8.6 %
B1421	7 kbar	1190	C	IW+1.24	−10.56		30.9	53 %	47.4	11.8	30.3	7.6	2.6		−0.02 %
B1402	8 kbar	1255	C	IW+1.13	−9.85		28.3	<1%	99.1				0.5		+1.4 %
B1403	8 kbar	1235	C	IW+1.19	−10.02		25.8	13 %	87.4	0.9	9.4		2.2		−0.5 %
B1400	10 kbar	1275	C	IW+1.22	−9.45		23.8	<1%	99.9				1.0		+1.1 %
B1399	10 kbar	1245	C	IW+1.31	−9.71		23.5	25 %	74.6	*	22.4		3.2		+0.17 %
B1398	10 kbar	1215	C	IW+1.40	−9.98		41.5	70 %	29.9	8.0	54.7		6.2		−0.2 %
B1401	13 kbar	1295	C	IW+1.39	−8.96		25.8	19 %	80.7		19.1		2.3		+0.1 %
B1404	13 kbar	1255	C	IW+1.51	−9.29		27.9	46 %	53.6		42.8		5.4		−0.4 %
B1407	13 kbar	1215	C	IW+1.63	−9.63		66.7	70 %	29.5	4.1	59.0		7.2		−0.5 %

* Trace amounts (a few crystals).
[a] Fe = Fe capsule in evacuated SiO_2 tube; Fe-Pt = Fe-Pt loops + CO_2/H_2 mix for oxygen fugacity control; C = Graphite capsules. IHPV = Internally Heated Pressure Vessel.
[b] Does not include T ± P ramp up time (typically 40 min to 1.5 hr for 1 atm experiments, 20 to 30 min for piston-cylinder experiments).
[c] Furnace failure sometime after 68.5hr. Despite slow cooling (relative to quench), mineral assemblages and core compositions similar to Dorb-5 (1132 °C) experiment.
[d] Spinel in Dorb-5 and -7 is magnetite (not observed in natural angrite specimen).
[e] Graphite capsule cracked and the melt touched the Pt capsule. With the exception of pure metal, the same mineral assemblages and compositions are observed in the piston cylinder experiment performed at similar P and T (B1412).

at the Iron-Quartz-Fayalite buffer (IQF ~ IW-0.6). As the Ol-Cpx-Plag equilibrium assemblage present in D'Orbigny was not observed at the liquidus under such reducing conditions, two series of runs were carried out at higher fO_2: IW+0.5 and QFM. For these 6 additional experiments, the sample powder was loaded on Fe+Pt loops using Elvanol and the fO_2 was fixed using a mixture of CO_2 and H_2 gases inside the furnace. The Fe+Pt loops, used to avoid problem of Fe-loss, were pre-saturated in Fe following Grove (1982). The samples were loaded in the furnace at ~ 980 °C and the temperature was increased to the run temperature over the next 60–90 min. The run temperatures were measured using a calibrated thermocouple placed in close proximity to the sample and are precise to within ± 1 °C. The oxygen fugacity was measured using an electrolyte solid cell inside the gas mixing furnace. At the end of the run (after 3–6 days, depending on the run), the experimental charges were quenched by being dropped in water. None of these 1 atm experiments yielded the Ol-Cpx-Plag equilibrium assemblage present in D'Orbigny. Therefore, a series of high-pressure experiments were undertaken to explore the effect of changing pressure on Ol-Cpx-Plag saturation.

3.3. Piston-cylinder experiments: 5 to 13 kbar

Ten piston-cylinder experiments (Table 4) were conducted in the MIT experimental petrology laboratory using a 12.7 mm end-loaded, solid medium, piston-cylinder device (Boyd and England, 1960). Following Médard et al. (2008), ~ 10 mg of the sample powder was loaded in a graphite crucible, which imposes an upper limit on oxygen fugacity at the graphite-carbon dioxide (CCO) buffer, above which graphite is not stable. Calibration of the exact fO_2 during such experiments yielded a value of CCO-0.8(±0.3) (Médard et al., 2008), which translates here to fO_2 values between IW+1.13 and IW+1.63 depending on the experimental P-T conditions (Table 4). The sample loaded graphite crucible, closed with a graphite lid, was placed inside of a platinum (Pt) capsule, and dried overnight at 300–330 °C in a pot furnace. The Pt capsule was then welded shut, inserted in an alumina (Al_2O_3) sleeve, and positioned in the center of a straight-walled graphite furnace using MgO spacers. The furnace itself was surrounded by a $BaCO_3$ pressure medium, which has been found to require no friction correction through calibration against the reaction Ca-Tschermak pyroxene = anorthite + gehlenite + corundum (Hays, 1966). The assembly was placed inside the piston-cylinder device, on top of a thin sealing graphite disk, and capped with a steel plug. A Tungsten-Rhenium thermocouple was inserted in the hollow portion of the steel plug and MgO spacer, and positioned on top of the graphite furnace to monitor the sample's temperature. Experiments were first pressurized to 10 kbar (or to the desired pressure, for experiments below 10 kbar) at room temperature, then heated to 865 °C at 100 °C/min, at which point the T was held constant for 3–5 min while the pressure was increased to the experimental pressure. The temperature was then increased to the experimental T at a rate of 50 °C/min. The samples were held at their final run conditions for 24–67 h, and the experiments were terminated by turning off the heating components while maintaining the cooling system on. In all runs, temperature readings remained stable within 1 °C. A temperature correction of +20 °C is applied to account for the difference in temperature between the hotspot and the thermocouple location. The temperature reproducibility inside the capsule is estimated at ± 10 °C. The pressure is thought to be accurate to within ± 0.5 kbar down to 8 kbar (Médard et al., 2008). The uncertainty on the pressure at 5 kbar has not been previously investigated.

In these high-pressure experiments, spinel replaces plagioclase as the stable Al-rich phase, and the 8 kbar experiments showed saturation in Ol + Cpx + Sp close to the liquidus. To complement the upper limit of 8–9 kbar thus obtained for the multiple saturation of a D'Orbigny-like melt, and to validate the results of the 5 kbar piston cylinder experiment, a series of experiments were also conducted using an IHPV (internally heated pressure vessels) setup, in which the pressure has been shown to be accurate to within ± 0.01 kbar with no correction (Berndt et al., 2002).

3.4. IHPV experiments: 3 to 5 kbar

Four IHPV experiments (Table 4) were conducted in large volume IHPV at the Institute of Mineralogy of the Leibniz University Hannover (Germany), using argon as the pressure medium. The ground starting material was packed into 3 mm inner diameter graphite capsule with top lid, and dried for 24 hr at 120–150 °C. The graphite capsule was placed into an outer 4 mm inner diameter Pt jacket welded shut with bottom and top Pt lids, before being fixed to a Pt-wire in the hot spot of the double-wire element furnace. Temperature was controlled using two S-type thermocouples while two additional S-type thermocouples were used to monitor the sample temperature. Temperature gradient across the sample is generally less than 5 °C. The vessel was pressurized cold to ~ 80 % of final pressure and then heated to the final temperature while pressure was slowly increased. Temperature was increased with a ramp of 0.8 °C/s to a temperature 30 °C lower than the final temperature and then 0.3 °C/s to the final temperature. Quenching was performed by fusing the Pt-wire and dropping the capsules onto a cold (~25 °C) copper block. Quench rate was ~ 150 °C/s.

3.5. Electron Probe X-ray Microanalyzer (EMPA)

Silicate phases in the experimental charges were analyzed using the JEOL JXA-8200 electron microprobe at MIT, with a 10nA beam current and a 15 kV accelerating potential. Beam diameter was set to 1 μm for minerals and highly crystalline runs in which only small pocket melts remained (*e.g.*, Dorb-8, B1398, B1407), and 10 μm for silicate glasses in low crystallinity runs. The CITZAF correction package of Armstrong (1995) was used to reduce the data. The atomic number correction of Duncumb and Reed, Heinrich's tabulation of absorption coefficients, and the fluorescence correction of Reed were used to obtain a quantitative analysis as outlined in Armstrong (1995). Analytical precisions were estimated during each analytical session through replicate analyses of well-characterized mineral standards, both synthetic (fayalite, forsterite, anorthite) and natural (olivine, orthopyroxene, clinopyroxene, hematite and spinel), as well as a basalt glass working standard (*e.g.*, Grove et al., 1992; Médard and Grove, 2008).

4. Results

For all experiments, a summary of the run conditions, duration, and the phase proportions is presented in Table 4. The target fO_2 values are calculated relative to the IW buffer using the parameterization of Huebner (1971), O'Neill (1987), O'Neill and Pownceby (1993), and Jakobsson and Oskarsson (1994). Electron microprobe analyses of the phases in each run are reported in Table 5.

4.1. One atmosphere experiments

Representative backscattered electron (BSE) images of the 1 atm runs are shown in Fig. 2, while the temperature and phase assemblages are shown in Fig. 3. Regardless of fO_2 conditions, near the liquidus, the experimental charges all present olivine (Fo 36.9–46.6) and anorthite (An 98.9–100), but no pyroxene is observed. In the reducing (silica-evacuated glass) experiments (IQF buffer, *i.e.*, IW-0.6) a hercynite-spinel (Fe# = 56) is present near the liquidus

Table 5
Analyses of the experimental charges.

Run	*n*	SiO_2	TiO_2	Al_2O_3	Cr_2O_3	FeO	MnO	MgO	CaO	P_2O_5	Sum	Mg#	$KD_{Fe\text{-}Mg}$
Dorb-3 (1 atm, 1173 °C, IW-0.57)													
oliv	10	35.3 (6)	0.03 (3)	0.08 (3)		39.0 (5)	0.31 (5)	25.1 (5)	1.36 (4)		101.2 (4)	53.4	0.302
plag	*Anorthite*												
spinel	8	0.08 (5)	0.45 (16)	60.3 (1.9)	2.66 (1.67)	26.4 (6)	0.13 (3)	11.5 (3)	0.14 (5)		101.6 (1.4)	43.7	0.446
glass	10	37.2 (2)	0.86 (5)	12.4 (1)	0.05 (3)	28.4 (2)	0.26 (3)	5.52 (13)	15.1 (1)	0.12 (3)	99.9 (4)	25.7	
Dorb-1 (1 atm, 1153 °C, IW-0.59)													
oliv	8	34.5 (4)	0.05 (3)	0.08 (1)		42.0 (4)	0.41 (5)	22.4 (3)	1.70 (9)		101.2 (6)	48.8	0.310
plag	6	43.1 (1.3)		35.6 (3)		1.26 (34)		0.13 (9)	20.3 (2)		100.4 (1.6)	16.0	
spinel	1	0.22	0.81	57.3	0.66	31.5	0.13	9.46	0.16		100.2	34.9	0.552
glass	9	37.0 (4)	1.01 (7)	11.2 (1)	0.02 (4)	29.0 (3)	0.29 (4)	4.81 (24)	15.9 (2)	0.19 (4)	99.4 (5)	22.8	
Dorb-2 (1 atm, 1133 °C, IW-0.61)													
oliv	9	33.9 (6)	0.03 (4)	0.07 (11)		44.3 (3)	0.40 (6)	20.1 (4)	2.21 (36)		101.0 (7)	44.7	0.317
plag	6	43.3 (7)		35.5 (6)		1.04 (36)		0.09 (2)	20.3 (2)		100.3 (1.3)	13.8	
Ca-oliv	8	34.6 (1.0)	0.09 (8)	0.09 (11)	0.03 (3)	44.9 (2.1)	0.41 (3)	20.0 (2.4)	2.30 (64)	0.01 (4)	102.4 (1.3)	44.3	0.322
glass	10	37.2 (3)	1.26 (9)	9.8 (1)	0.04 (4)	29.5 (2)	0.27 (3)	4.25 (5)	16.9 (1)	0.22 (3)	99.6 (5)	20.4	
Dorb-4 (1 atm, 1113 °C, IW-0.63)													
oliv	8	33.3 (5)	0.05 (3)	0.04 (2)		46.2 (4)	0.44 (7)	18.3 (4)	2.58 (16)		100.9 (6)	41.3	0.289
plag	7	43.5 (3)		36.2 (3)		0.98 (19)		0.09 (2)	20.1 (2)		100.8 (7)	13.6	
glass	9	37.2 (7)	1.42 (7)	9.26 (18)	0.04 (3)	30.1 (3)	0.26 (3)	3.43 (37)	18.3 (6)	0.26 (4)	100.3 (6)	16.9	
Dorb-11 (1 atm, 1094 °C, IW-0.65)													
oliv	10	33.4 (2)	0.06 (4)	0.04 (2)	0.03 (6)	47.6 (7)	0.40 (5)	15.1 (2)	3.90 (17)	0.01 (3)	100.6 (6)	36.2	0.299
plag	*Anorthite*												
cpx	8	47.0 (9)	1.42 (32)	6.65 (1.51)	0.32 (19)	12.7 (9)	0.13 (3)	8.90 (53)	23.7 (2)		100.8 (1.1)	55.5	0.136
glass	5	36.6 (5)	1.79 (4)	8.64 (9)	0.02 (4)	30.2 (1)	0.24 (3)	2.87 (22)	19.3 (4)		99.7 (3)	14.5	
Dorb-9 (1 atm, 1136 °C, IW+0.5)													
oliv	8	35.2 (7)	0.06 (2)	0.04 (2)		38.8 (7)	0.46 (7)	24.3 (7)	1.53 (4)		100.4 (6)	52.7	0.336
plag	4	43.1 (7)		34.8 (1.0)		1.12 (29)		0.13 (10)	19.5 (2)		98.7 (1.6)	17.4	
glass	10	40.4 (6)	1.24 (4)	9.99 (15)	0.06 (5)	25.0 (3)	0.30 (3)	5.27 (19)	17.1 (2)		99.4 (8)	27.3	
Dorb-10 (1 atm, 1120 °C, IW+0.5)													
oliv	10	33.1 (6)	0.08 (4)	0.05 (2)		47.4 (8)	0.54 (9)	17.2 (7)	2.36 (9)		100.7 (7)	39.3	0.340
plag	5	42.5 (1.0)		35.5 (1.0)		1.53 (69)		0.08 (4)	19.9 (2)		99.6 (2.4)	8.6	
cpx	10	48.7 (1.2)	0.94 (22)	5.32 (1.45)	0.28 (8)	12.5 (8)	0.15 (3)	9.86 (75)	23.6 (3)		101.3 (7)	58.5	0.156
glass	3	37.6 (1.1)	2.15 (20)	8.78 (16)	0.52 (5)	30.3 (1.2)	0.51 (2)	3.74 (7)	16.1 (1.1)	0.44 (7)	100.1 (8)	18.1	
Dorb-8 (1 atm, 1106 °C, IW+0.5)													
oliv	7	32.8 (4)	0.06 (6)	0.09 (16)		50.2 (1.0)	0.53 (9)	13.9 (6)	3.17 (22)		100.8 (7)	33.0	0.368
plag	3	43.1 (8)		35.3 (5)		1.21 (17)		0.06 (1)	19.8 (2)		99.5 (1.6)	8.0	
cpx	6	46.2 (1.4)	1.59 (17)	6.80 (51)	0.22 (14)	13.3 (3)	0.11 (3)	8.56 (23)	23.6 (3)		100.5 (1.1)	53.4	0.158
glass	2	36.2 (2.5)	2.55 (98)	8.32 (79)	0.27 (74)	30.8 (1.1)	0.39 (36)	3.13 (41)	18.6 (5)		100.3 (4)	15.3	
Dorb-6 (1 atm, 1163 °C, IW+3.56)													
oliv	7	36.3 (1.0)	0.02 (3)	0.07 (3)		32.2 (6)	0.35 (5)	30.9 (8)	1.02 (8)		100.8 (1.7)	63.1	0.313*
plag	4	43.0 (4)		34.0 (1.7)		2.82 (2.24)		0.50 (46)	19.7 (4)		100.0 (7)	24.0	
spinel	8	0.17 (17)	1.01 (13)	35.4 (1.9)	6.92 (1.96)	46.2 (1.2)	0.18 (4)	8.57 (52)	0.34 (11)		98.8 (8)	24.8	1.399
glass	19	39.1 (4)	0.92 (5)	11.6 (2)	0.01 (2)	25.5 (1)	0.27 (4)	6.61 (17)	15.2 (2)		99.3 (5)	31.6	
Dorb-7 (1 atm, 1151 °C, IW+3.57)													
oliv	7	35.0 (1.2)	0.03 (2)	0.10 (19)		38.1 (7)	0.45 (5)	26.2 (6)	1.28 (18)		101.2 (1.3)	55.1	N/A
plag	1	43.9		35.8		1.64		0.16	20.0		101.5	14.7	
cpx	6	47.6 (1.2)	0.53 (15)	6.4 (1.1)	0.04 (7)	12.5 (6)	0.13 (3)	10.7 (5)	22.6 (4)		100.4 (5)	60.5	N/A
glass	*N/A (See Table 4 for details)*												
Dorb-5 (1 atm, 1132 °C, IW+3.59)													
oliv	7	34.8 (8)	0.04 (1)	0.05 (1)		39.3 (7)	0.48 (5)	24.5 (1.0)	1.30 (17)		100.5 (1.4)	52.6	0.328*
plag	4	43.2 (3)		34.9 (0.6)		1.58 (34)		0.15 (5)	19.7 (3)		99.5 (8)	14.8	
cpx	19	47.6 (1.3)	0.51 (11)	5.46 (1.03)	0.05 (4)	12.1 (4)	0.13 (2)	11.1 (5)	22.3 (3)		99.2 (8)	62.1	0.188
spinel	9	0.30 (22)	5.87 (30)	10.3 (6)	0.56 (52)	73.4 (9)	0.21 (3)	2.93 (24)	0.31 (16)		93.9 (7)	6.6	4.339
glass	6	38.6 (6)	1.22 (7)	9.36 (26)	0.03 (5)	28.4 (1)	0.32 (3)	4.91 (20)	15.4 (1)	0.32 (8)	98.6 (7)	23.6	
IHPV-1 (3 kbar, 1160 °C, IW+1.81)													
oliv	7	35.2 (2)	0.04 (3)	0.11 (18)	0.06 (4)	39.8 (6)	0.35 (6)	25.2 (3)	1.44 (16)		102.2 (7)	53.1	0.319
plag	*Anorthite*												
glass	10	38.3 (7)	1.08 (6)	11.2 (3)	0.003 (18)	26.3 (3)	0.28 (8)	5.33 (20)	16.1 (2)	0.17 (8)	98.8 (1.1)	26.5	
IHPV-2 (5 kbar, 1190 °C, IW+1.88)													
oliv	6	36.0 (2)	0.04 (2)	0.03 (2)	0.02 (2)	36.1 (3)	0.28 (8)	27.4 (2)	1.13 (4)	0.03 (4)	101.0 (6)	57.5	0.325
spinel	3	0.18 (8)	0.23 (4)	61.1 (4)	2.38 (68)	24.0 (5)	0.14 (3)	13.1 (1)	0.23 (3)		101.3 (7)	49.2	0.452
glass	6	39.6 (1)	0.82 (4)	12.8 (1)	0.003 (11)	24.5 (3)	0.27 (3)	6.02 (8)	15.9 (1)	0.16 (3)	100.0 (4)	30.5	
B1412 (5 kbar, 1170 °C, IW+0.5)													
oliv	8	34.4 (3)	0.02 (2)	0.05 (2)	0.005 (12)	42.3 (3)	0.48 (9)	22.8 (3)	1.49 (6)		101.5 (3)	49.0	0.305
plag	*Anorthite*												
cpx	15	47.2 (1.2)	0.70 (15)	7.73 (1.55)	0.36 (15)	10.6 (6)	0.13 (3)	10.9 (9)	23.0 (4)		100.7 (1.3)	64.6	0.160
glass	8	38.7 (1.3)	1.23 (6)	10.7 (4)	0.02 (4)	28.2 (5)	0.31 (3)	4.64 (20)	16.3 (2)	0.23 (4)	100.3 (1.9)	22.6	
IHPV-3 (5 kbar, 1170 °C, IW+1.94)													
oliv	10	34.7 (9)	0.06 (7)	0.16 (49)	0.04 (4)	43.7 (4)	0.68 (11)	22.0 (8)	0.92 (4)		102.2 (6)	47.3	0.316
plag	*Anorthite*												
cpx	9	48.2 (1.3)	0.82 (20)	6.73 (2.05)	0.06 (4)	12.5 (1.1)	0.21 (10)	10.6 (1.0)	21.5 (1.4)		100.7 (8)	60.2	0.188
glass	2	40.0 (7)	2.35 (3)	11.1 (5)		27.8 (8)	0.59 (18)	4.44 (10)	12.4 (5)	0.52 (22)	99.2 (1)	22.1	
IHPV-4 (5 kbar, 1170 °C, IW+1.94)													

Table 5 (*continued*)

Run	*n*	SiO_2	TiO_2	Al_2O_3	Cr_2O_3	FeO	MnO	MgO	CaO	P_2O_5	Sum	Mg#	KD_{Fe-Mg}
oliv	2	34.9 (1)	0.02 (5)	0.03 (1)		42.9 (1)	0.56 (10)	21.4 (6)	1.23 (17)		101.1 (8)	47.1	0.345
plag	*Anorthite*												
cpx	6	46.5 (1.3)	0.76 (15)	9.89 (1.27)	0.16 (3)	10.8 (3)	0.13 (3)	10.0 (5)	22.5 (2)		100.8 (7)	62.3	0.186
spinel	2	2.07 (58)	0.44 (12)	60.9 (4.1)	0.76 (94)	27.8 (3)	0.17 (6)	10.4 (4)	0.91 (37)		103.5 (1.4)	40.0	0.462
glass	6	40.1 (3)	1.67 (4)	11.2 (1)		27.6 (2)	0.46 (6)	4.76 (27)	13.7 (3)	0.40 (4)	99.9 (5)	23.5	
B1421 (7 kbar, 1190 °C, IW+0.5)													
oliv	7	33.9 (3)	0.07 (3)	0.13 (20)		48.4 (4)	0.45 (4)	17.5 (1)	1.58 (9)		102.0 (4)	39.3	0.310
plag	*Anorthite*												
cpx	14	45.4 (6)	0.95 (19)	10.5 (9)	0.10 (6)	12.8 (4)	0.15 (3)	8.80 (52)	22.2 (3)		100.9 (4)	55.0	0.164
spinel	5	0.15 (11)	0.75 (13)	58.0 (4)	0.76 (45)	34.8 (1.3)	0.18 (5)	7.57 (56)	0.17 (21)		102.4 (1.0)	28.0	0.516
glass	11	36.8 (5)	1.37 (7)	10.8 (6)	0.01 (3)	31.6 (7)	0.28 (6)	3.54 (23)	14.7 (2)	0.37 (15)	99.4 (7)	16.7	
B1402 (8 kbar, 1255 °C, IW+0.5)													
spinel	1	0.21	0.25	61.3	2.40	24.2	0.13	12.7	0.24		101.5	48.4	0.487
glass	10	38.9 (2)	0.86 (5)	12.3 (1)	0.01 (3)	25.9 (3)	0.25 (3)	6.65 (6)	14.9 (2)	0.15 (9)	99.9 (6)	31.4	
B1403 (8 kbar, 1235 °C, IW+0.5)													
oliv	5	35.0 (4)	0.02 (1)	0.07 (2)		38.6 (6)	0.35 (5)	26.1 (5)	1.02 (1)		101.1 (5)	54.7	0.308
cpx	7	48.4 (8)	0.38 (6)	6.89 (95)	0.05 (3)	10.5 (3)	0.14 (2)	12.0 (6)	22.2 (4)		100.6 (9)	67.1	0.182
spinel	9	0.16 (9)	0.27 (6)	60.3 (1.6)	1.22 (75)	26.3 (3)	0.14 (3)	11.6 (5)	0.29 (8)		100.3 (9)	44.0	0.474
glass	8	38.8 (2)	0.92 (4)	12.3 (1)	0.03 (4)	26.8 (3)	0.28 (4)	5.60 (6)	14.8 (2)	0.18 (4)	99.7 (3)	27.1	
B1400 (10 kbar, 1275 °C, IW+0.5)													
spinel	4	0.23 (7)	0.21 (1)	61.5 (5)	2.18 (36)	24.4 (5)	0.12 (2)	12.3 (5)	0.17 (9)		101.1 (4)	47.4	0.523
glass	8	38.6 (2)	0.84 (6)	11.9 (1)	0.01 (2)	25.5 (3)	0.24 (3)	6.73 (11)	15.0 (1)		98.8 (4)	32.0	
B1399 (10 kbar, 1245 °C, IW+0.5)													
oliv	2	34.7 (1)	0.04 (6)	0.11 (4)		41.4 (1)	0.38 (13)	23.4 (2)	0.97 (2)		101.0 (5)	50.2	0.332
cpx	9	46.8 (1.2)	0.46 (9)	9.38 (1.51)	0.06 (4)	11.5 (4)	0.13 (2)	11.0 (9)	21.7 (3)		101.0 (7)	63.1	0.195
spinel	8	0.34 (81)	0.29 (6)	59.2 (9)	0.44 (27)	28.7 (6)	0.15 (3)	10.6 (3)	0.35 (57)		100.1 (6)	39.6	0.508
glass	10	37.5 (3)	1.01 (5)	11.5 (1)	0.04 (3)	29.5 (4)	0.31 (2)	5.53 (8)	14.0 (1)		99.4 (5)	25.0	
B1398 (10 kbar, 1215 °C, IW+0.5)													
oliv	8	32.6 (6)	0.05 (4)	0.07 (2)		53.7 (9)	0.51 (6)	13.6 (7)	0.96 (9)		101.4 (5)	31.1	0.373
cpx	10	45.2 (5)	0.70 (8)	10.5 (9)	0.04 (3)	16.2 (5)	0.17 (3)	7.74 (28)	21.1 (3)		101.8 (8)	45.9	0.198
spinel	8	0.25 (18)	0.74 (11)	56.9 (1.1)	0.26 (20)	36.7 (8)	0.19 (2)	5.87 (30)	0.29 (9)		101.3 (9)	22.2	0.590
glass	8	37.5 (9)	1.66 (50)	11.3 (5)	0.19 (51)	33.4 (1.5)	0.44 (21)	3.15 (23)	12.1 (4)		99.7 (2.3)	14.4	
B1401 (13 kbar, 1295 °C, IW+0.5)													
cpx	8	45.7 (7)	0.40 (6)	10.8 (1.4)	0.05 (5)	10.8 (5)	0.14 (2)	10.6 (5)	21.4 (4)		99.9 (5)	63.7	0.207
spinel	8	0.16 (4)	0.26 (5)	59.1 (1.0)	0.57 (24)	27.8 (2)	0.14 (3)	10.8 (3)	0.20 (6)		99.0 (9)	40.9	0.527
glass	9	36.9 (6)	0.98 (7)	11.3 (1)		28.2 (2)	0.28 (2)	5.76 (12)	13.8 (2)		97.2 (5)	26.7	
B1404 (13 kbar, 1255 °C, IW+0.5)													
cpx	10	45.0 (6)	0.42 (7)	9.6 (0.9)	0.05 (5)	14.5 (1.1)	0.19 (4)	9.08 (29)	19.8 (4)		98.6 (8)	52.7	0.224
spinel	10	0.28 (21)	0.48 (6)	55.9 (8)	0.31 (20)	33.4 (5)	0.17 (2)	7.97 (35)	0.19 (15)		98.7 (7)	29.8	0.587
glass	9	36.3 (3)	1.16 (6)	10.3 (3)	0.004 (14)	32.3 (4)	0.32 (3)	4.51 (11)	11.9 (1)	0.28 (12)	97.1 (7)	19.9	
B1407 (13 kbar, 1215 °C, IW+0.5)													
oliv	10	32.5 (4)	0.02 (2)	0.09 (4)		52.5 (6)	0.48 (10)	14.1 (4)	0.90 (10)		100.6 (6)	32.4	0.335
cpx	11	44.9 (6)	0.57 (12)	9.83 (57)	0.05 (3)	16.7 (5)	0.22 (4)	7.75 (33)	19.6 (3)		99.6 (1.0)	45.3	0.193
spinel	10	0.28 (25)	0.83 (6)	53.7 (9)	0.23 (9)	38.0 (4)	0.17 (3)	5.95 (19)	0.24 (9)		99.4 (6)	21.8	0.574
glass	2	36.9 (5)	1.53 (9)	10.2 (4)	0.03 (1)	35.8 (3)	0.36 (3)	3.22 (18)	11.4 (4)		99.5 (1.1)	13.8	

Number in parentheses is the 2SD of mean of replicate analyses. KD_{Fe-Mg} is for oliv/liq, cpx/liq and spinel/liq.

* For the QFM experiments, the amount of Fe^{3+} in the liquid is non-negligible (Fe^{3+}/Fe^{2+} ~14–15 %, Kress & Carmichael 1991). The K_D values, which are technically defined as $(Fe^{2+}/Mg^{2+})_{oliv}/(Fe^{2+}/Mg^{+2})_{liq}$, were thus adjusted accordingly, and it is the corrected value which is reported.

(1173 °C) but reacts away at lower T (below ~1150 °C). In contrast, in the most oxidized experiments (QFM buffer, *i.e.*, IW+3.5), the more hercynitic spinel (Fe# = 75) initially present near the liquidus (1163 °C) is replaced by magnetite at lower T (below ~1150 °C). In all experiments, a fassaitic pyroxene only appears far from the liquidus, after ~40–50 % of crystallization. The Ol-melt equilibrium exchange coefficients between Fe and Mg, $K_{D_{Ol-liq}^{Fe-Mg}}$, calculated from the composition of equilibrium olivine cores and the glass, are 0.289–0.317, 0.336–0.368, and 0.313–0.328 respectively, for experiments performed under IQF, IW+0.5 and QFM fO_2 conditions.

When the positions of the saturation boundaries observed in the 1 atm experiments are plotted in the pseudoquaternary Ol-Cpx-Plag-Qtz diagrams, the dependency on oxygen fugacity is clearly visible (Fig. 4a). As fO_2 increases, the saturation boundary moves away from the Cpx corner and towards the quenched Group 2 cluster. Nevertheless, even under the most oxidizing conditions tested (QFM), none of the 1 atm experiments fully reproduce the quenched Group 2 cluster position. Such oxidizing conditions are unrealistic for the APB as magnetite would become a major stable phase, similar in abundance to olivine (Table 4), a feature that is not observed in quenched angrite specimens, indicating that more reducing conditions prevailed on the APB, and as pointed out by previous work (*e.g.*, Brett et al., 1977; Mckay et al., 1994; Shearer et al., 2016; Steenstra et al., 2017).

4.2. High-pressure experiments

Representative BSE images of the IHPV and piston-cylinder runs are shown in Fig. 5. The temperature, pressure and phase assemblages are summarized in the phase diagram shown in Fig. 6. In most experiments, FeO loss/gain is minimal (<~0.5 %), indicating that the charges behaved as closed systems. The three main exceptions are the 5 kbar IHPV experiments (IHPV-2, -3 and -4; Table 4) in which significant FeO loss is observed (from 2.4 to 12.3 %), and pure FeO is visible in the charge (Fig. 5). We suspect that for these experiments, the Pt capsules were not correctly sealed and/or opened during the experiment, allowing the fO_2 to deviate from the ~ IW+2 target and reach significantly more reducing conditions at which Fe metal is stable.

As best seen in Fig. 6, at low pressures (from 1 atm to 5 kbar) the Ol + Cpx + Plag saturation occurs increasingly closer to the liquidus as pressure increases. At 5 kbar, all three phases are present ~ 20–30 °C below the liquidus (~29 % crystallization). At

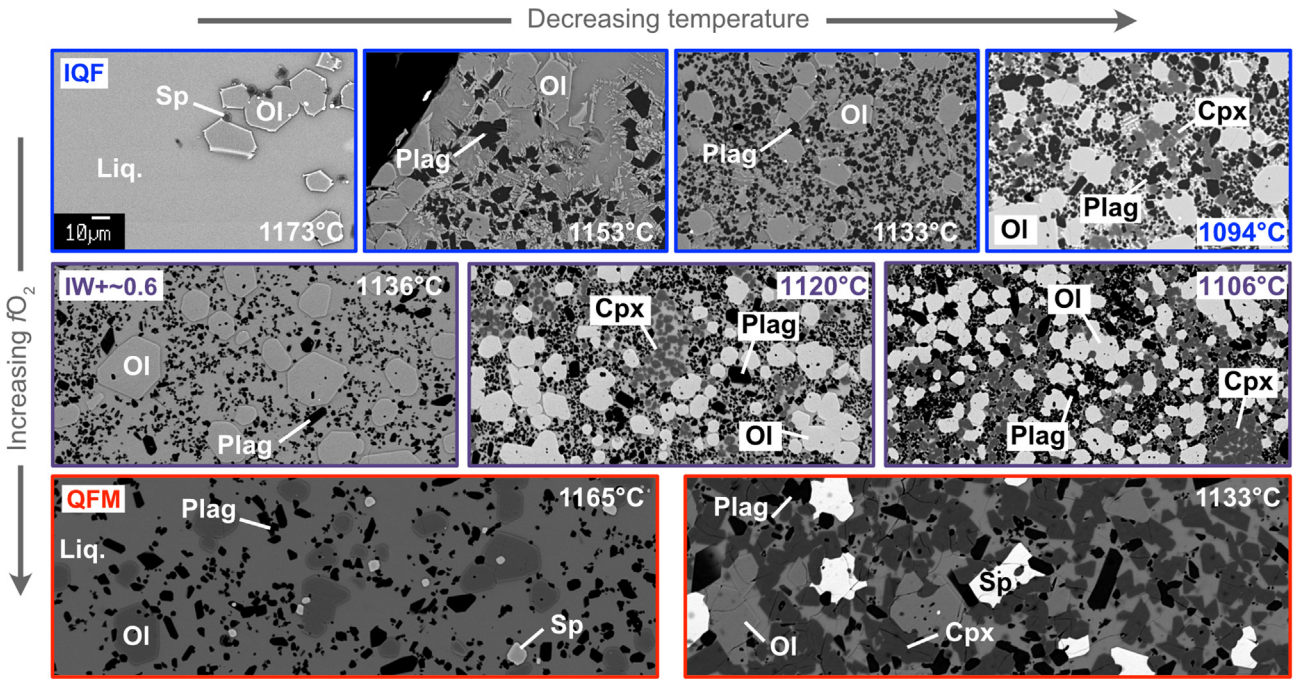

Fig. 2. Representative BSE images of selected 1 atm experiments. Temperature decreases towards the right and oxygen fugacity increases towards the bottom. The 10-µm scale bar shown in the top left panel applies to all images. From left to right, top row: Dorb-3, -1, -2 and -11; center row: Dorb-9, -10, and -8; bottom row: Dorb-6 and -5. Note the large abundance of magnetite in Dorb-5 (bottom right panel); a phase not present in the natural D'Orbigny angrite.

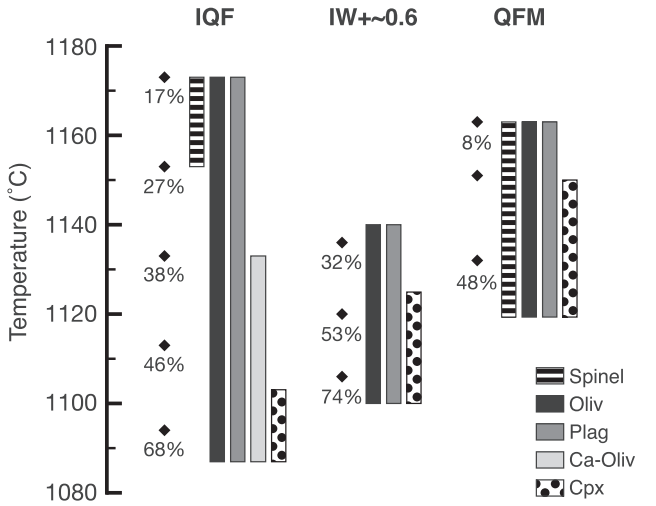

Fig. 3. Temperature and phase assemblages in the 1 atm experiments. Top labels refer to the oxygen fugacity of the experiments and percent values to crystallinity of the run. While the synthetic powder used has the composition of the D'Orbigny angrite, the Ol + Cpx + Plag assemblage observed in the natural specimen is not observed near the liquidus, regardless of the fO_2 conditions.

this same pressure, however, the Ol + Cpx + Plag saturation is still not yet achieved near the liquidus, and only olivine (and trace amounts of spinel) is observed in the experimental charge. While piston-cylinder experiments are rarely calibrated at such low pressures, and therefore seldom used, we find that the IHPV and piston-cylinder experiments performed under similar conditions (5 kbar, 1170 C, IW+~1.5) present similar textures, and their mineral assemblages have virtually identical compositions (see experiments IHPV-3, IHPV-4 and B1412; Table 5), indicating that the piston-cylinder experiments at 5 kbar are reliable and equivalent to the IHPV experiments. However, because experiments IHPV-3 and -4 suffered large FeO losses (12.3 and 8.6 %, respectively) compared to piston-cylinder experiment B1412 (0.3 % loss), the latter will be favored in the discussion.

As P increases above 5 kbar, the melts pass through a four-phase equilibrium saturation Ol + Cpx + Plag + Sp, starting at ~ 6 kbar with the appearance of spinel and ending at ~ 7.5 kbar with the disappearance of plagioclase. The experiment performed at 7 kbar showed saturation in Ol + Cpx + Plag + Sp and a high degree of crystallization (53 %) despite being only 20 °C below the liquidus, which is consistent with multiple saturation near the liquidus in those P-T conditions (*i.e.*, large amount of crystallization over a short temperature interval). Similarly, the experiment performed at 8 kbar and within 10 °C of the liquidus is highly crystallized (13 %) and multiply saturated in Ol + Cpx + Sp (plagioclase is no longer stable in those conditions). In both cases, Ol + Cpx + Sp (±Plag) saturation at the liquidus seems to have been achieved. At higher pressures (10 and 13 kbar), experimental runs are no longer multiply saturated in Ol + Cpx + Sp near the liquidus, as the melt moves from the Liq + Ol + Cpx + Sp field to the Liq + Cpx + Sp field with increasing temperature.

When the composition of the glasses measured in these experiments are plotted in the pseudoquaternary Ol-Cpx-Plag-Qtz diagrams, a match with the quenched Group 2 cluster (*i.e.*, D'Orbigny-like composition) is only obtained for the 7–8 kbar runs (Fig. 4b). Experiments at 5 kbar (and below) are offset towards the Cpx corner, while experiments at 10 kbar and above are offset towards the Ol corner. Collectively, our experiments indicate that a pressure of ~ 6–9 kbar is necessary for saturation in Ol + Cpx + Sp (±Plag) for a melt of D'Orbigny composition crystallizing under redox conditions close to the IW buffer.

5. Discussion

5.1. Two related groups of quenched angrites

As discussed in Section 2, the growing number of angrite specimens reveals that quenched angrites define two compositionally

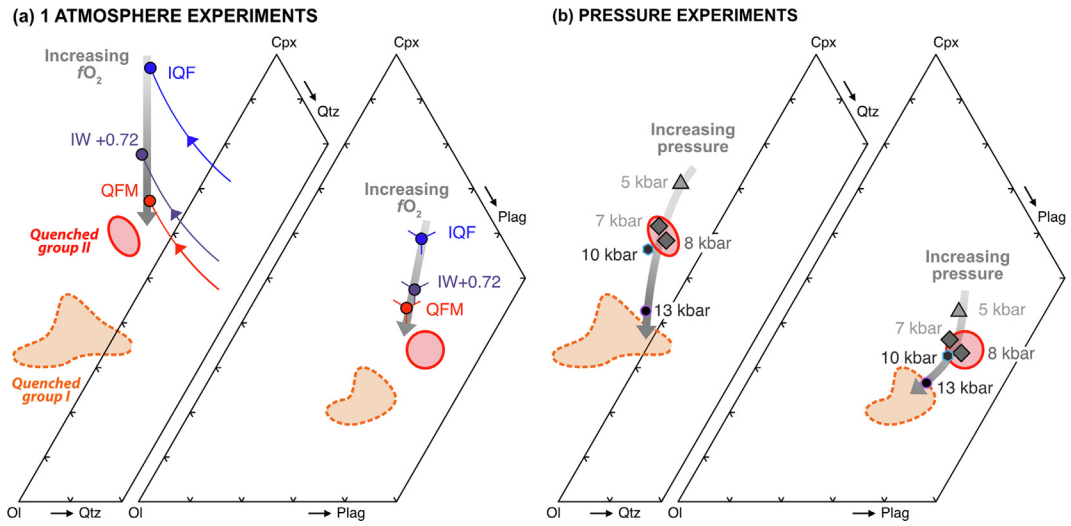

Fig. 4. Pseudoternary Ol-Cpx-Qtz and Ol-Cpx-Plag projections showing the position of the Ol-Cpx-Plag saturation boundary at different oxygen fugacities (a) and pressures (b), as established by the glass composition of the experiments when all three phases are first present. The dependency on oxygen fugacity is clearly visible but regardless of fO_2, none of the experiments fully reproduce the quenched Group 2 cluster position. In contrast, at 7–8 kbar, the experiments perfectly match the Group 2 composition.

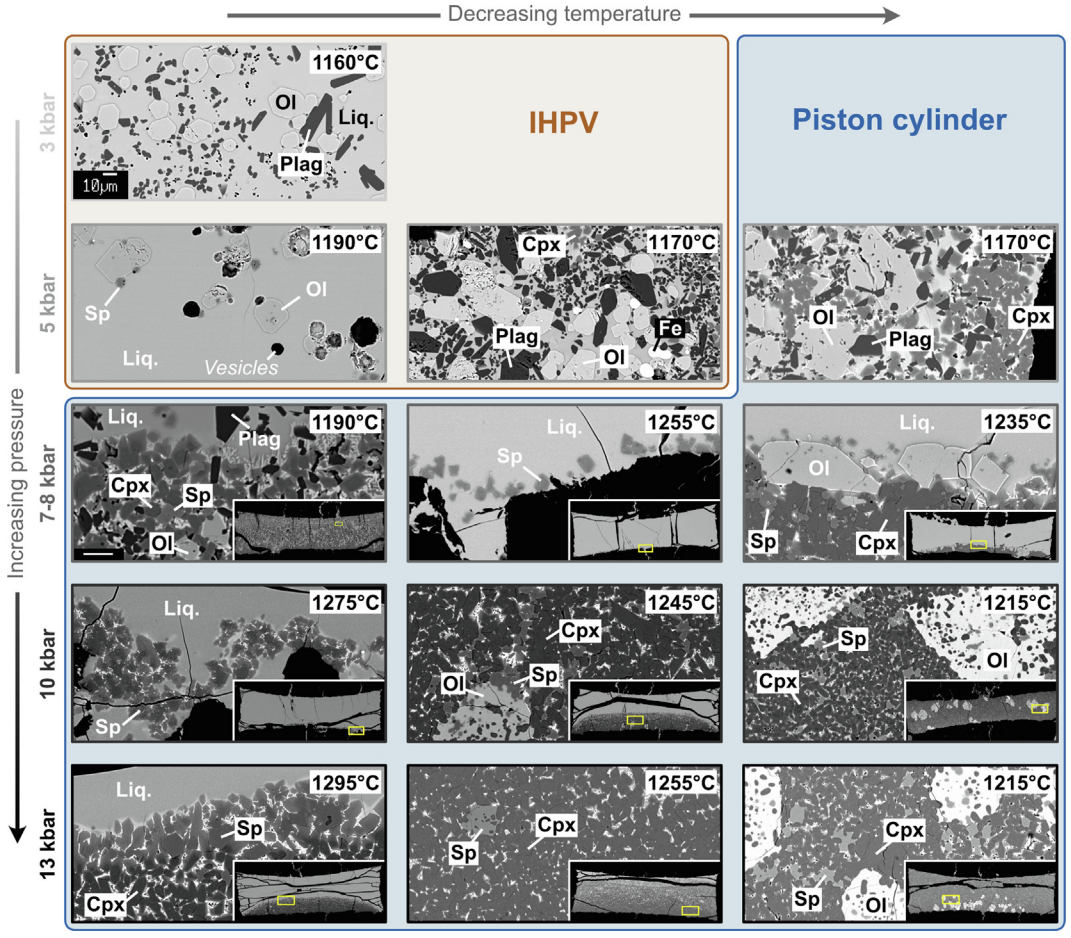

Fig. 5. Representative BSE images of selected high-pressure experiments. Temperature decreases towards the right and pressure increases towards the bottom. The 10-µm scale bar in the top left panel applies to all images except B1421 (middle row, left column), which is 2x magnified (see 10-µm scale bar in that panel).

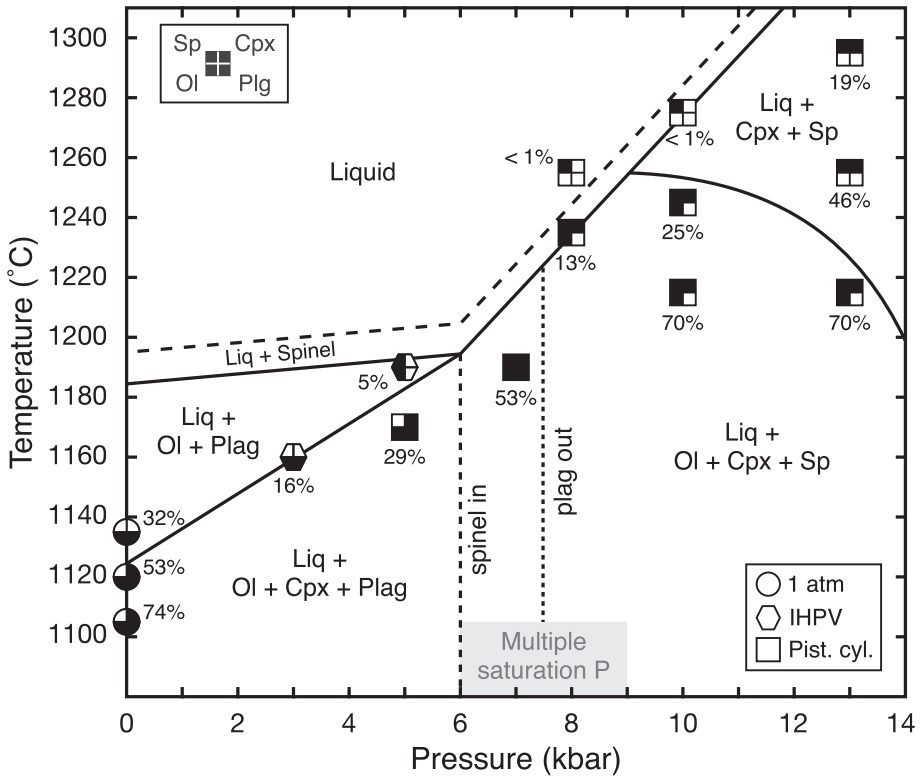

Fig. 6. P-T conditions of the experiments conducted on the synthetic D'Orbigny composition. Piston cylinder experiments are shown as squares, IHPV experiments as hexagons and 1 atm experiments conducted in similar fO_2 conditions (~IW+0.5) as circles. In each symbol, a filled (open) quadrant denotes the presence (absence) of the corresponding phase. The slopes of the phase boundaries are from the experimental literature on MORB compositions (Tormey et al., 1987; Grove and Bryan, 1983; Grove et al., 1992) and correspond to: ~10 °C / 6 kbar for the liquidus over the 0 to 6 kbar range; 10–11 °C / kbar for the Liq + Ol + Plag to Liq + Ol + Plag + Cpx boundary over the 0 to 6 kbar range; ~20 °C / kbar for the liquidus over the 6 to 12 kbar range. As too few constraints exist on the plagioclase to spinel transition in natural systems (Obata, 1976), this boundary is shown as a dashed vertical line.

distinct groups (Fig. 1). Based on the tight clustering of quenched Group 2 specimens in the pseudoquaternary Ol-Cpx-Plag-Qtz diagrams, we initially hypothesized (i) that the quenched Group 2 angrites sit on an Ol + Cpx + Sp (±Plag at low pressure) multiple saturation boundary, and (ii) that quenched Group 1 angrites might represent the primitive melts from which Group 2 specimens formed, for instance, through fractional crystallization. Under these assumptions, the sequence of crystallization going from the Group 1 to Group 2 angrites would be Ol, followed by Ol + Plag, and finally, once the melts have reached the multiple saturation boundary, Ol + Plag + Cpx.

To test this hypothesis, we performed forward and reverse equilibrium fractional crystallization calculations, in 2 % liquid mass increment, and assuming no reequilibration between the solid and melt. At each step, the composition of the equilibrium solid phase(s) is calculated using the models of Grove et al. (1992), Yang et al. (1996), and Till et al. (2012), and the results are shown graphically in Fig. 7 (see Supplementary Table S1 for more details). Forward crystallization calculations, starting from the average composition of LEW 87051 and NWA 1670, on the one hand, and Asuka 881371 and LEW 87051 on the other hand, provide decent matches to the average composition of quenched Group 2 specimens (Fig. 7a-b). The reverse fractional crystallization calculation yields a composition nearly identical to that of angrite LEW 87051 and the average of quenched Group 1 angrites (Fig. 7c-d). These illustrative calculations clearly demonstrate that the two groups of quenched angrites can be related through fractional crystallization and originated from similar source magmas.

While the major element composition of quenched Group 1 and 2 angrites indicate that they evolved from similar parental melts, trace elements abundances, in particular REEs, allow us to rule out direct linkages between known specimens in the two groups. That is, they did not evolve from the *exact same* magma. Indeed, using REE mineral-melt equilibrium partition coefficients relevant to angrite for olivine, plagioclase and clinopyroxene (see Supplementary Table S2), in combination with the degree of fractional crystallization between quenched Group 1 and 2 angrites derived above (Table S1), we can model the REE pattern and enrichment levels in quenched Group 2 angrites. We find that, while the modeled REE patterns remain flat (*i.e.*, chondritic), the modeled enrichment levels are about 30 % higher than those in the natural samples (~20 × CI, instead of 14 × CI) (Fig. 8a). This observation indicates that quenched Group 1 and 2 angrites originated from similar, yet distinct, reservoirs on the APB.

5.2. Relationship between quenched and plutonic angrites

Despite their partial cumulate textures, some of the plutonic angrites have bulk compositions relatively close to those of quenched angrites (Fig. 1). For instance, LEW86010 and NWA 10463 could represent quenched Group 2 melts with excess Cpx (±Plag). On the other hand, NWA 2999 and NWA 4931 could represent primitive (quenched Group 1) compositions with excess olivine. Similarly, and after subtraction of an exogenous metal component (Baghdadi et al., 2015), NWA 3164 and NWA 5167 have bulk compositions within the field of primitive (quenched Group 1) angrites.

Here, we integrate petrological observations on plutonic angrites and the results of our fractional crystallization modeling to test whether some of the plutonic angrites originated from par-

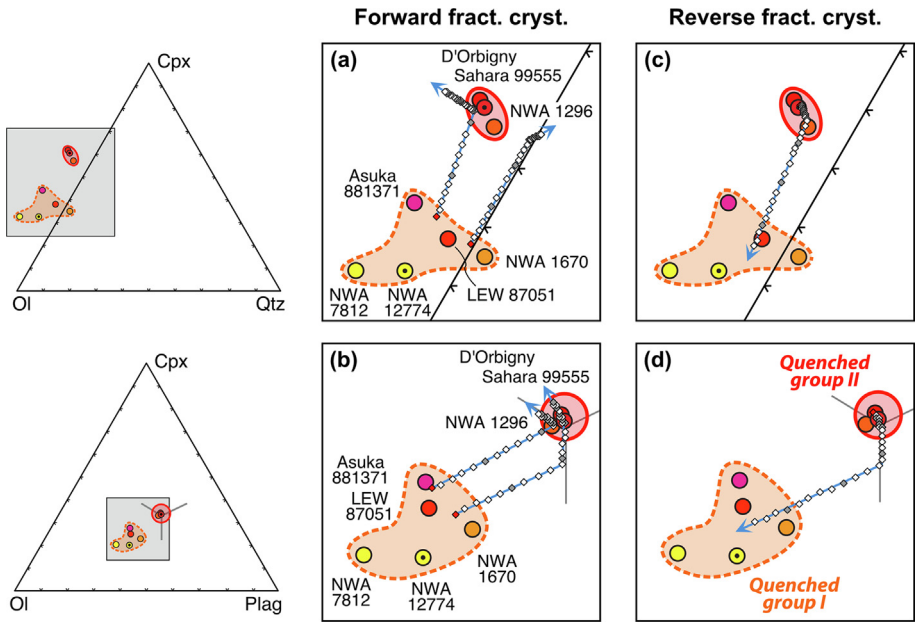

Fig. 7. Close up view of the pseudoternary Ol-Cpx-Qtz (a and c) and Ol-Cpx-Plag (b and d) projections showing the compositions of quenched Group 1 and 2 angrites, and the fractional crystallization model trajectories. Forward models are shown in panel (a) and (b) and reverse models in panels (c) and (d). The two groups of quenched angrites can easily be related by fractional crystallization.

ental melts similar to those of quenched angrites. Specifically, we consider angrites LEW 86010, NWA 4801 and NWA 4950, for which mineral modes (Crozaz and McKay, 1990; Sanborn, 2012), as well as REE abundances in whole rock (Table 6) and individual mineral phases (Crozaz and McKay, 1990; Sanborn and Wadhwa, 2021) are available. We assume that the primitive melt from which these samples evolved had an REE pattern and enrichment similar to quenched Group 1 angrites (we use Asuka 881371, for which the whole REE pattern is available). For each sample, we use the Mg# of the most magnesian cpx (~73.6 to 74.4) and a $K_{D^{Fe-Mg}_{Cpx-liq}}$ of 0.24 to calculate the Mg# of the equilibrium melt from which the first Cpx in the rock crystallized (~40.1 to 41.1). Varying the K_D value to cover the range observed in our high-pressure experiments (0.18–0.24), has only a small impact on the modeled pattern enrichment level. Using the fractional crystallization models shown in Table S1, we find the step along the crystallization path that matches the melt Mg# and, using the REE K_D values in Table S2 and the REE content in Asuka 881371, we calculate the REE pattern and enrichment of the residual melt. At this point, the patterns are chondritic, at ~ 16 × CI, and the residual melts are plotting on the multiple saturation boundary, where closed-system crystallization would yield Ol/Cpx/Plag modal abundances of ~30/38/32 %. We then compare these values to the Ol-Cpx-Plag modal abundances of the three plutonic angrites, and using the average REE abundances in the relevant mineral phases, attempt to account for the cumulate nature of these rocks by simply adding the extra amount of each mineral phase needed.

To first-order, LEW 86010 and NWA 4801 contain, respectively, ~25 % and ~60 % excess Cpx compared to the residual melt matching their magnesian Cpx Mg#, while NWA 4590 contains both 12 % excess Ol and 9 % excess Cpx. Adding the corresponding REE content to the modeled residual melt yields the modeled REE patterns shown in Fig. 8b-d. We find very good agreement between the measured and modeled whole rock REE patterns, both in terms of pattern and enrichment level: within 10 % for NWA 4801 and 30 % for LEW 86010. For the NWA 4590, the average enrichment is well matched, but a lower LREE abundance is not captured by our modeling, suggesting a more complex cumulate evolution for this sample. Nevertheless, this exercise indicates that to first-order, some plutonic angrites share the same general magmatic evolution as quenched Group 2 angrites, and their compositional offset from the multiple saturation boundary only reflects their slight cumulate nature. In this context, the trend in Lu concentrations (used as a proxy for REE enrichments and by extension, magmatic evolution) vs ages in plutonic angrites revealed by our compilation work (Fig. 9), could reflect a combination of crystallization of a main silicate reservoir on the APB (*i.e.*, magma ocean crystallization), and accumulation of olivine (NWA 2999 and paired specimen, such as NWA 6291) or clinopyroxene (±plag) (LEW 86010, NWA 4801, NWA 4590, and AdoR), in agreement with the cumulate nature of these samples.

5.3. The APB's bulk composition and core size

5.3.1. The nebular vs parent body processing debate

We now consider the major outstanding question of the APB's bulk composition, and by extension, the size of its core. Angrites are silica-undersaturated basalts and the most volatile-depleted (and refractory-enriched) meteorites known to date, displaying K/U and Rb/Sr ratios 100 × lower than the Bulk Silicate Earth and 500 × lower than CI chondrites (Halliday and Porcelli, 2001; Dauphas et al., 2022). Whether this volatile depletion is a primitive feature or the result of processing of the APB remains highly debated. Initial studies proposed that the APB consisted in a mixture of components observed in meteorites: CAI-type materials and Fe-bearing silicates (Delaney and Sutton, 1988) or opaque matrix from chondrites (Prinz et al., 1988). Similarly, Longhi (1999) observed that the APB could have formed by incomplete

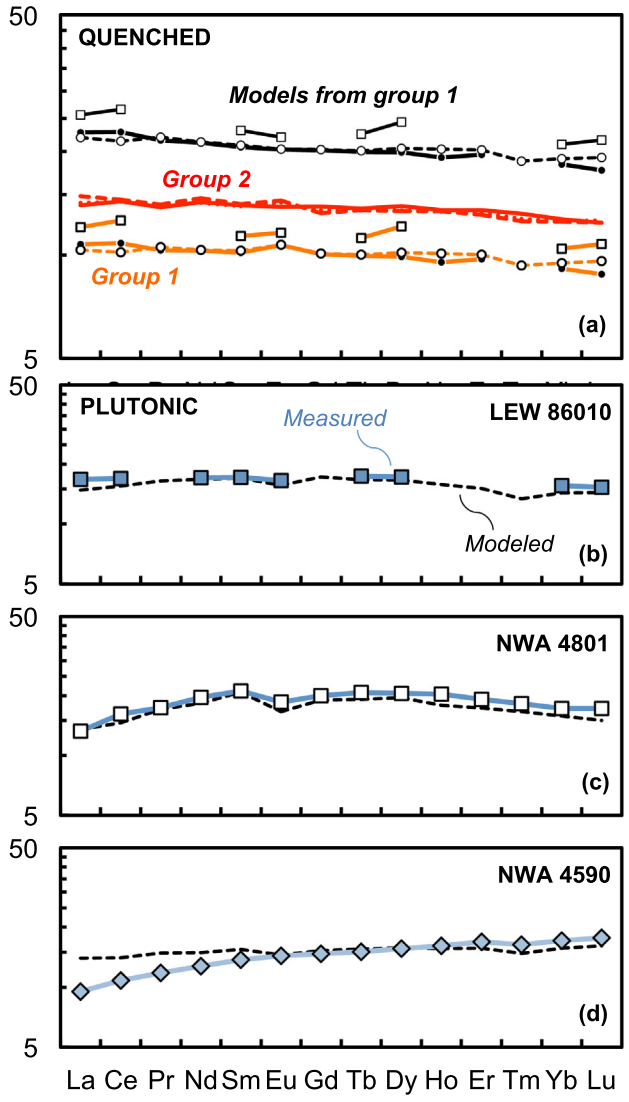

Fig. 8. Whole rock REE abundances in angrites, and calculated equilibrium melts. (a) Quenched Group 1 abundances, ~10 × CI, are shown in orange (open circle: Asuka 881371; filled circle: NWA 1670; open square: LEW 87051). Quenched Group 2 abundances, ~14 × CI, are shown in red (solid line: NWA 1296; dashed line: D'Orbigny; dotted line: Sahara 99555). Theoretical melts, evolved from quenched Group 1 compositions using the steps shown in Table S1, are shown in black. (b-d) Whole-rock and modeled REE pattern for plutonic angrites LEW 86010, NWA 4801 and NWA 4590. Good agreement is observed between the measured and modeled patterns, except for the light REEs for NWA 4590, indicating a more complex evolution history than that assumed by our modeling for this sample.

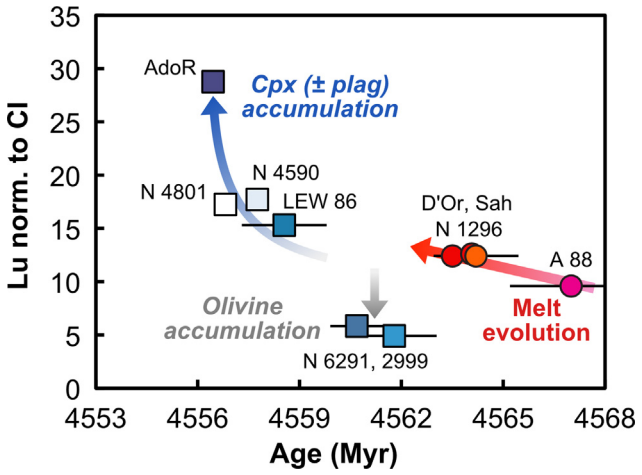

Fig. 9. Lu concentrations vs Pb-Pb ages of angrites. Symbols as in Fig. 1. Concentration data from Table 6. For D'Orbigny, NWA 4590, NWA 4801, NWA 6291, AdoR and Sahara 99555, ages are U-corrected Pb-Pb ages from Tissot et al. (2017). For the other samples, only uncorrected dates are available: LEW 86010 (Amelin, 2008), NWA 1296 and NWA 2999 (Amelin and Irving, 2007), and Asuka 881371 (Premo and Tatsumoto, 1995). For high-precision uncorrected Pb-Pb dates, a conservative uncertainty of ± 1.25 Myr is shown (the largest age offset due to U isotope variations in angrites, Tissot et al. 2017).

mixing between an (hypothetical) alkali-depleted primitive chondrite from which metal had been removed, with a low-SiO_2 high-T condensate (*e.g.*, CAI, amoeboid olivine aggregates: AOAs). A nebular control was also invoked by Papike et al. (2017), who observed, based on Mn-Fe trends in olivines, that the APB volatile depletion could reflect formation from partial condensates from a hot vapor cloud.

Instead of such nebular origin, Crozaz and McKay (1990) argued that volatile depletion associated with extensive igneous processing (*e.g.*, parent-body formation, magmatic activity) of a chondrite-like parent body (possibly enriched in refractory elements), better explained the major features of angrites, including the presence of FeO in plutonic angrites AdoR and LEW 86010. Similarly, Mittlefehldt and Lindstrom (1990) proposed that the high FeO/MnO ratios of angrites and their low Na (volatile) content reflected outgassing during differentiation of an APB of bulk composition akin to carbonaceous chondrites (CI, CM, or CO). In this model, the superchondritic Ca/Al ratio of angrites (*i.e.*, refractory enrichment) would simply reflect residual aluminous spinel in the source regions of angrites (Mittlefehldt and Lindstrom, 1990; Mittlefehldt et al., 2002; McKibbin and O'Neill, 2018). This hypothesis has been the subject of a series of experiments aimed at producing angritic melt by partial melting of chondrites (*e.g.*, Jurewicz et al., 1991, 1993, 1995, 2004). These showed that partial melting of Allende powder at 1200 °C under oxidizing conditions (IW+2) can produce a melt with major element composition closely matching that of quenched Group 2 angrites (D'Orbigny, Sahara 99555). Significant differences remained in the minor element, in particular, a higher Mn and lower Na content in D'Orbigny relative to the partial melts produced from Allende, which the authors suggested reflect actual features of the APB (Jurewicz et al., 2004). More recently, McKibbin and O'Neill (2018) pointed out that the distinct isotopic anomalies in angrites and CV chondrites (*e.g.*, Warren, 2011; Charlier et al., 2017; Budde et al., 2019) precluded a direct genetic link between the two materials, and proposed that the APB composition was made of CV-like materials (*i.e.*, refractory enriched) via processing in early high-T nebular, magma ocean, or impact environments. By observing that the large majority of early formed meteorite parent bodies from the "non-carbonaceous" group were alkali-rich, Collinet and Grove (2020) suggested that angrites became alkali-depleted following igneous differentiation or impacts.

Two alternative, and more controversial, scenarios have also been proposed to explain the unique compositional and textural features of angrites. The first model proposes a non-magmatic origin whereby D'Orbigny, and other angrites, would have formed by direct condensation from a vapor phase with solar composition. This would explain the high Ca/Al ratio and low SiO_2 content of angrites, as well as the presence of vesicles, open druses and abundant glass in D'Orbigny, and proponents of this model argue that angrites "*can be seen as CAIs, which grew larger than the ones we know from carbonaceous chondrites*" (Kurat et al., 2004; Varela et al., 2003, 2005, 2017). The second model posits, based on the puzzling presence of magmatic carbonate in NWA 1296, that the

Table 6
Compilation of REEs concentrations in whole rock angrites (in ppm). When multiple estimates available, preferred values in bold font.

Sample	Mass (mg)	Ba	La	Ce	Pr	Nd	Sm	Eu	Gd	Tb	Dy	Ho	Er	Tm	Yb	Lu	Hf	Th	U	Ref.
Plutonic angrites																				
AdoR	660	35	7.3	19		15.6	5.9	1.94		1.35	8.7				5.1	0.73	2.6	0.55	0.13	[1]
AdoR	52	36	6.14	19.2		16.3	5.76	1.78		1.39					4.82	0.69	2.79	0.64		[2]
AdoR	50.5	**20.9**	**6.2**	**18.5**	**3.09**	**17.2**	**5.9**	**1.81**	**7.3**	**1.39**	**9.2**	**2.03**	**5.6**	**0.83**	**5.0**	**0.72**	**2.70**	**0.74**	**0.20**	**[3]**
±		**0.3**	**0.2**	**0.3**	**0.04**	**0.3**	**0.1**	**0.07**	**0.2**	**0.05**	**0.3**	**0.08**	**0.2**	**0.03**	**0.1**	**0.01**	**0.07**	**0.05**	**0.01**	
LEW 86010	55	48	3.38	10.1			2.68	0.978		0.66					2.64	0.386	2.21	0.48		[2]
LEW 86010	190	51	4.7	10.9		8.1	2.60	0.97			4.4				2.61	0.38	1.87	0.40	0.15	[1]
LEW 86010 avg		**49.5**	**4.04**	**10.5**		**8.1**	**2.64**	**0.974**		**0.66**	**4.4**				**2.63**	**0.383**	**2.04**	**0.44**	**0.15**	**[1–2]**
NWA 2999	167	220	0.80	2.0		<7	0.67	0.236		0.177					0.77	0.120	0.58	<0.2	0.13	[4]
±		140	0.52	1.0			0.14	0.038		0.032					0.08	0.010	0.12		0.14	
NWA 2999	613.1		**0.614**	**2.133**	**0.354**	**1.990**	**0.649**	**0.238**	**0.925**	**0.166**	**1.127**	**0.252**	**0.753**	**0.110**	**0.787**	**0.123**				**[5]**
±			**0.031**	**0.107**	**0.018**	**0.099**	**0.032**	**0.012**	**0.046**	**0.008**	**0.056**	**0.013**	**0.038**	**0.006**	**0.039**	**0.006**				
NWA 3164	450	171	1.39	3.43	0.573	3.10	1.04	0.408	1.40	0.248	1.65	0.350	1.04		1.02	0.155	0.875	0.030	0.337	[6]
NWA 4931	50.8	72.5	0.522	1.72	0.299	1.89	0.69	0.39	0.93	0.183	1.26	0.284	0.82	0.132	0.88	0.141	0.72	0.028	0.032	[3]
±		0.2	0.003	0.01	0.006	0.01	0.01	0.01	0.02	0.004	0.03	0.007	0.02	0.002	0.03	0.003	0.02	0.002	0.002	
NWA 5167	500	160	0.48	1.59	0.290	1.71	0.652	0.290	0.956	0.170	1.18	0.267	0.80		0.87	0.135	0.697	0.028	0.019	[6]
NWA 6291	~33/645*		0.485	1.682	0.323	2.100	0.765	0.298	1.094	0.196	1.333	0.299	0.891	0.131	0.933	0.146		0.483	0.139	[7]
NWA 4590	50.3	81	3.19	8.8	1.35	7.42	2.61	1.06	3.51	0.70	4.9	1.14	3.32	0.52	3.31	0.50	2.2	0.325	0.096	[3]
±		2	0.04	0.1	0.01	0.09	0.05	0.03	0.07	0.02	0.1	0.02	0.07	0.01	0.07	0.01	0.5	0.009	0.004	
NWA 4590	~37/738*		2.044	6.230	1.092	5.950	2.212	0.896	3.402	0.616	4.312	0.966	3.066	0.462	3.290	0.504		0.364	0.126	[7]
NWA 4590	737.5		1.652	5.034	0.882	4.785	1.511	0.579	2.200	0.398	2.787	0.624	1.982	0.299	2.072	0.326				[5]
±			0.083	0.252	0.044	0.239	0.076	0.029	0.110	0.020	0.139	0.031	0.099	0.015	0.104	0.016				
NWA 4590 avg		**81**	**2.295**	**6.688**	**1.108**	**6.052**	**2.111**	**0.845**	**3.037**	**0.571**	**4.000**	**0.910**	**2.789**	**0.427**	**2.891**	**0.443**	**2.2**	**0.345**	**0.111**	**[3,5,7]**
NWA 4801	50.1	40.5	3.43	10.68	1.75	10.0	3.46	1.152	4.43	0.844	5.60	1.22	3.388	0.507	3.106	0.460	2.564	0.283	0.094	[3]
±		0.6	0.01	0.06	0.01	0.1	0.03	0.008	0.04	0.005	0.05	0.01	0.007	0.001	0.001	0.002	0.008	0.004	0.001	
NWA 4801	50.8	36.2	2.96	9.3	1.52	8.6	3.02	1.03	3.85	0.733	4.90	1.08	2.95	0.4422	2.72	0.404	2.24	0.242	0.081	[3]
±		0.8	0.07	0.1	0.03	0.2	0.08	0.01	0.05	0.009	0.05	0.01	0.01	0.0004	0.07	0.006	0.03	0.002	0.001	
NWA 4801	~31/611*		1.848	5.600	0.938	5.180	1.834	0.602	2.688	0.448	2.870	0.616	1.764	0.238	1.596	0.224		0.182	0.070	[7]
NWA 4801	611.2		2.199	6.664	1.116	6.131	2.233	0.716	2.682	0.533	3.416	0.733	2.099	0.283	1.883	0.267				[5]
±			0.110	0.333	0.056	0.307	0.112	0.036	0.134	0.027	0.171	0.037	0.105	0.014	0.094	0.013				
NWA 4801		**38.35**	**3.195**	**9.990**	**1.635**	**9.300**	**3.240**	**1.091**	**4.140**	**0.789**	**5.250**	**1.150**	**3.169**	**0.475**	**2.913**	**0.432**	**2.402**	**0.263**	**0.088**	**[3]**
Quenched angrites																				
Asuka 881371	50.3	23	2.50	6.3	0.99	4.9	1.58	0.63	2.09	0.38	2.60	0.57	1.66	0.243	1.60	0.24	1.24	0.33	0.082	[3]
±		1	0.06	0.1	0.03	0.1	0.06	0.02	0.04	0.01	0.08	0.02	0.06	0.009	0.06	0.01	0.09	0.02	0.005	
D'Orbigny	55.88/200**	47	3.56	8.78		nd	2.161	0.846		0.534					2.12	0.309	1.63	0.370	<0.210	[8]
±		18	0.04	0.26			0.029	0.016		0.019					0.06	0.013	0.06	0.040		
D'Orbigny	53.34	52	3.76	9.18		5.4	2.23	0.876		0.511					2.13	0.308	1.48	0.434	0.116	[8]
±		7	0.04	0.24		2.6	0.03	0.017		0.018					0.04	0.007	0.05	0.029	0.022	
D'Orbigny	50.5	50.01	3.753	9.22	1.331	6.92	2.15	0.840	2.718	0.508	3.384	0.760	2.15	0.3328	2.09	0.31560	1.58	0.454	0.082	[3]
±		0.02	0.002	0.04	0.009	0.01	0.02	0.007	0.004	0.002	0.009	0.004	0.01	0.0003	0.02	0.00001	0.02	0.009	0.001	
D'Orbigny	65.8	49.35	3.425	8.943	1.301	6.953	2.169	0.858	2.756	0.499	3.479	0.752	2.178	0.321	2.120	0.307	1.552	0.451	0.077	[3]
D'Orbigny	~36/728*		3.727	10.255	1.695	8.937	3.157	0.971	4.112	0.770	4.915	1.058	3.141	0.433	3.001	0.46		0.454	0.081	[7]
D'orbigny avg		**48.79**	**3.579**	**8.981**	**1.316**	**6.937**	**2.160**	**0.848**	**2.737**	**0.514**	**3.432**	**0.756**	**2.164**	**0.327**	**2.110**	**0.311**	**1.587**	**0.425**	**0.080**	**[3,7,8]**
LEW 87051	13		2.32	6.2			1.48	0.536		0.36					1.52	0.239	1.17	0.22		[2]
LEW 87051	27	<60	3.5	9.4			2.01	0.83		0.49	3.1				2.00	0.30	1.34	0.41	<0.21	[1]
LEW 87051 avg			**2.91**	**7.80**			**1.75**	**0.68**		**0.43**	**3.1**				**1.76**	**0.27**	**1.26**	**0.32**		**[1.2]**
NWA 1296	63.3	40.78	3.333	9.097	1.295	7.079	2.222	0.845	2.88	0.527	3.685	0.801	2.317	0.344	2.23	0.325	1.593	0.451	0.067	[3]
NWA 1296	360	168	3.40	8.65	1.29	6.44	2.06	0.780	2.84	0.509	3.42	0.726	2.16		2.06	0.296	1.46	0.43	0.070	[6]
NWA 1296 avg			**3.367**	**8.874**	**1.293**	**6.760**	**2.141**	**0.813**	**2.86**	**0.518**	**3.553**	**0.764**	**2.239**	**0.344**	**2.15**	**0.311**	**1.527**	**0.441**	**0.069**	**[3,6]**
NWA 1670	250	47.3	2.59	6.70	0.97	4.88	1.56	0.629	2.08	0.377	2.53	0.538	1.61		1.54	0.220	1.12	0.33	0.075	[6]
NWA 7812		126	2.06	12.0***	0.88	4.92	1.39	0.58	1.88	0.33	2.26	0.49	1.49	0.21	1.37	0.21	1.5			[9]
Sahara 99555	28.89/522**	45.0	3.20	8.41		nd	2.107	0.829		0.512					2.12	0.319	1.80	0.360	<0.210	[8]
±		17.0	0.04	0.24			0.028	0.018		0.023					0.04	0.009	0.06	0.040		
Sahara 99555	46.1	37.27	3.536	9.01	1.285	6.70	2.127	0.821	2.70	0.505	3.40	0.76	2.16	0.332	2.11	0.322	1.63	0.50	0.106	[3]
±		0.03	0.005	0.02	0.004	0.05	0.004	0.008	0.05	0.006	0.03	0.01	0.02	0.002	0.01	0.002	0.02	0.02	0.003	

(*continued on next page*)

Table 6 (*continued*)

Sample	Mass (mg)	Ba	La	Ce	Pr	Nd	Sm	Eu	Gd	Tb	Dy	Ho	Er	Tm	Yb	Lu	Hf	Th	U	Ref.
Sahara 99555	290	31.7	3.54	9.16	1.34	6.74	2.16	0.860	2.87	0.519	3.49	0.748	2.23		2.11	0.305	1.51	0.45	0.097	[6]
Sahara 99555 avg		**38.0**	**3.425**	**8.860**	**1.313**	**6.720**	**2.131**	**0.837**	**2.785**	**0.512**	**3.445**	**0.754**	**2.195**	**0.332**	**2.11**	**0.315**	**1.647**	**0.437**	**0.102**	**[3,6,8]**
Diabasic angrites																				
NWA 12004		80.9	3.64	9.27	1.39	6.86	2.17	0.85	2.95	0.50	3.48	0.75	2.19		2.07	0.311				[10]
NWA 12320		83.1	3.31	8.45	1.26	6.20	1.98	0.78	2.67	0.46	3.18	0.69	2.02		1.92	0.287				[10]

References: [1] Warren & Kallemeyn (1990), INAA. [2] Mittlefehldt & Lindstrom (1990), INAA. [3] Riches et al. (2012), ICPMS. [4] Gellissen et al. (2007), INAA. [5] Sanborn & Wadhwa (2021), ICPMS. [6] Baghdadi et al. (2015), ICPMS. [7] Tissot et al. (2017), ICPMS. [8] Mittlefehldt et al. (2002), INAA. [9] Irving et al. (2013), ICPMS on wire-saw cutting dust. [10] Irving et al. (2019), ICPMS on wire-saw cutting dust.

* Post dissolution split (numerator) from a larger mass digested as a whole (denominator).

** Powder split (numerator) from an homogenized mass (denominator).

*** Anomaly requiring further work to be confirmed.

elevated Ca/Al ratio in angrites is the results of melting in the presence of a carbonates (Jambon et al., 2005, 2008).

5.3.2. Support for the nebular hypothesis

Here, we argue that two key observations provide strong support for a nebular control on the bulk composition and volatile depletion of angrites, and in fact provide novel constraints on the composition of the APB. First is the fact that the ratios of major (refractory, non-siderophile) elements in chondrites define a nebular trend (see dashed lines and grey envelops in Fig. 10a-c), whereby the enrichment in refractory elements increases from enstatite to ordinary to carbonaceous chondrites (EC < OC < CC). Importantly, while the fits and error envelops shown in Fig. 10 are defined using only the chondrite data (see Supplementary Table S3), the high- and low-T components derived from equilibrium condensation calculations of a gas of solar composition at 10^{-3} bar (Morbidelli et al., 2020) plot on this nebular trend in Mg/Si vs Al/Si, Ca/Si and Ti/Si spaces, reinforcing the interpretation that this trend testifies to a first-order nebular control on the composition of Solar System materials. In Fig. 10, both the 1400 K and 1280 K "first condensates" and corresponding "residual condensates" are shown. In each case, the "first condensates" integrate the matter condensed all the way down to the threshold T (1400 K or 1280 K), with the matter condensing below this threshold T and down to 830 K forming the corresponding "residual condensate". For the refractory elements shown in Fig. 10, both the 1400 K and 1280 K condensates and residues fall on the nebular trend. The composition of AOAs – which are high-T condensates formed early in the history of the Solar System (Ruzicka et al., 2012) – and most types of chondrules also plot on (or close to) the nebular trend defined by chondrites, and further support the idea that this trend captures a first-order control on the composition of Solar System materials. As such, it is reasonable to assume that a nebular origin for the APB would require the APB to plot on that same nebular trend.

Second is the fact that, while plutonic angrites tend to have cumulate textures and will see their bulk composition controlled by the amount of cumulate phases they incorporated, quenched angrites with minimal xenocryts content will preserve the composition of their parental melt. Specifically, we here leverage the recognition that quenched Group 1 angrites represent such primitive angritic melts (Section 5.1). During equilibrium melting, and assuming the source melted to a large extent, the parental melt of these quenched Group 1 angrites would leave behind a residual mantle mainly made of olivine, the composition of which can be calculated using well-documented equilibrium partitioning coefficients (*e.g.*, Toplis 2005, Spandler and O'Neill, 2010; Blundy et al., 2020). This implies that, to first-order, the ratios of major lithophile elements in the APB corresponds to a mixture between those in a primitive melt of quenched Group 1 composition and its corresponding equilibrium olivine (yellow symbols in Fig. 10). Combining these two observations implies that, under the assumption of a nebular origin, the composition of the APB will lie at the intersection of the nebular trend defined by chondrites and the tie-lines between angritic primitive melts and their equilibrium olivine.

5.3.3. Implications for the APB's bulk composition and core size

We first consider the ratios of refractory and moderately refractory elements (*i.e.*, with 50 % condensation temperatures, Tc, above 1350 K, Lodders, 2003): Mg/Si, Al/Si, Ca/Si and Ti/Si. In these ratio spaces, the intercepts of the nebular trend and the primitive angrite Ol-melt tie-lines define tight domains (red contours in Fig. 10). Furthermore, in all three spaces, a unique Mg/Si atomic ratio, of ~1.3, is retrieved. This feature demonstrates the self-consistency of the APB composition thus obtained. Interestingly, a similar APB Mg/Si ratio of 1.31 ± 0.09 has been proposed based on a nebular trend between Mg/Si ratios and δ^{30}Si in chondrites

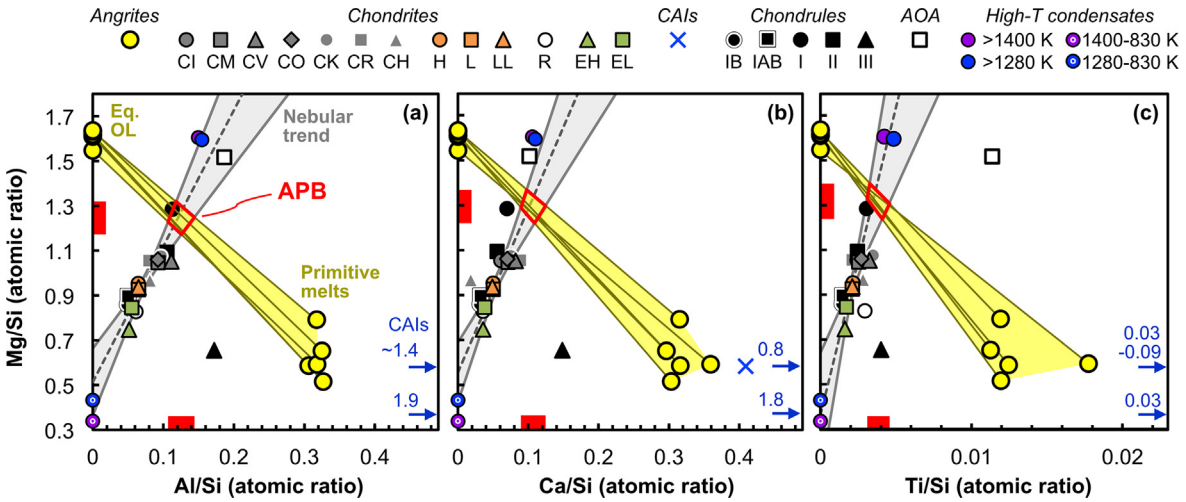

Fig. 10. Mg/Si ratio vs (a) Al/Si, (b) Ca/Si, and (c) Ti/Si showing the relationship between angritic primitive melt and their equilibrium olivine (yellow symbols) and chondrites and chondritic components (all other symbols, see legend). Nebular trends (grey dashed lines and 95 % CI envelops) are defined using ordinary, enstatite, and most carbonaceous chondrites. Some carbonaceous chondrites are omitted from the regressions (CV for Al/Si; CV, CR, CH for Ca/Si; and CV, CK, CH for Ti/Si), as they clearly depart from the general trend defined by all other chondrites, testifying to secondary control on their composition (*e.g.*, high CAI content in CVs, high-T reprocessing of CHs, Hezel et al., 2003). Component compositions are given in Table S3.

(Dauphas et al., 2015). The remarkable agreement between these two values, one derived using only the major element composition and the other combining elemental and isotopic compositions, further strengthens the hypothesis of a nebular control on the abundance of refractory to moderately refractory elements in the APB. Indeed, the Mg/Si ratio of ~1.3 derived for the APB is significantly higher than those of chondrites (between 0.75 and 1.08) and displaced toward the high Mg/Si ratio (~1.52 to 1.60) of high-T condensates, both theoretical (Morbidelli et al., 2020) and natural (AOAs).

Of the moderately volatile elements present in minor abundance in most meteorites (Cr, K, P, Na), only Cr defines a (broad) nebular trend with refractory and moderately refractory elements (Fig. 11a). Unlike for refractory elements, where both the 1400 K and 1280 K first and residual condensates fall on the nebular trend defined by chondrites, in Mg/Si vs Cr/Si space only the 1280 K condensate and residue fall on this trend. In stark contrast, the 1400 K condensates and residues define a separate, and orthogonal trend. This is partly because Cr is both moderately volatile (Tc ~1300 K) and moderately siderophile, and partly because the 1280 K condensates and residues are calculated under more reducing conditions (C/O ~0.9) than the 1400 K condensates and residues (which assume a solar C/O ratio of ~0.54; Asplund et al. 2009). Therefore, while no Cr has condensed in the first condensate at 1400 K, it is quantitatively removed from the gas phase into the first condensate (silicate and iron) at 1280 K under more reducing conditions (Morbidelli et al., 2020). As seen in Fig. 11a, in the Mg/Si vs Cr/Si space, the angrite Ol-melt tie-lines do not intersect the chondritic nebular trend at Mg/Si ~1.3. Instead, the angrite Ol-melt tie-lines intersect the theoretical nebular trend defined by the 1400 K condensate and residue at Mg/Si ratios of ~1.4–1.6. This indicates that the composition of the APB is dominated by material condensed before quantitative condensation of Cr: *i.e.*, at T > ~1300 K. The slightly elevated Mg/Si ratio (1.4–1.6) obtained in the Mg/Si vs Cr/Si space compared to the ~1.3 value obtained when considering lithophile refractory elements (Fig. 10) could be explained by the moderately siderophile nature of Cr during core formation, which will move the Ol-melt tie-lines towards lower Cr/Si values (Fig. 11a). To first-order, the bulk APB Cr/Si ratio can thus be retrieved by projecting the Mg/Si of ~1.3 onto the 1400 K condensate-residue tie-line, yielding a Cr/Si ratio of ~0.007–0.008.

We now consider the Fe/Si ratio of the APB, and by extension, the size of the APB core. While the Fe/Si ratios in primitive angrites (quenched Group 1) and their equilibrium olivine are virtually identical, and cluster around a value of ~0.36 to 0.54, this value

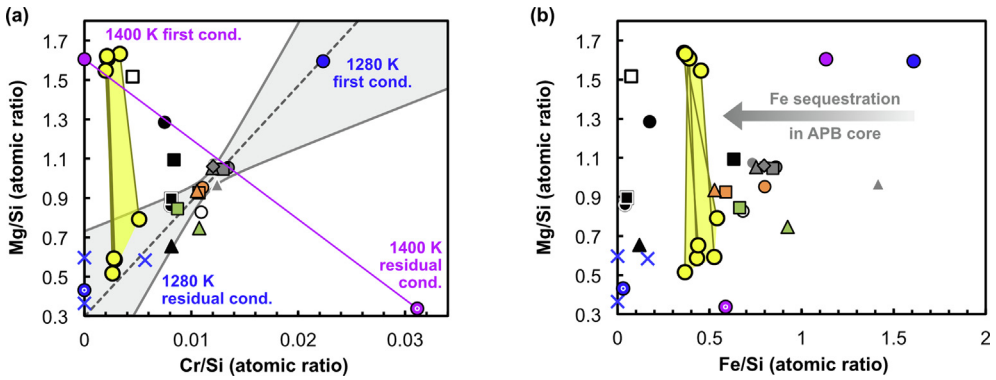

Fig. 11. Mg/Si ratio vs (a) Cr/Si, and (b) Fe/Si. Symbols as in Fig. 10, and compositions from Table S3. In panel (a), the grey dashed line and 95 % CI envelop is a regression through all chondrite data.

only provides an estimate of the Fe/Si of the APB mantle (*i.e.*, silicate portion) (see Fig. 11b). Like for Cr, a first-order estimate of the Fe/Si ratio of the bulk APB can be obtained by projecting the Mg/Si ratio of ~1.3 onto the 1400 K condensate-residue tie-line, which yields a value of ~1. This corresponds to ~46 to 64 % of Fe removal into the APB core, or a core representing ~17–23 wt% of the APB.

The above values are, of course, dependent on the APB Mg/Si ratio assumed (~1.3) and the projection of this ratio on the tie-line between the 1400 K first and residual condensates. We recognize that the later assumption might be too stringent. To more conservatively estimate the Fe/Si ratio and core size of the APB, we therefore relaxed this assumption and allowed the APB composition to be represented by 2-component mixtures between some high-T components (1400 K condensate, 1280 K condensate, AOAs) and low-T components (EH, EL, H, and LL chondrites, Type IB and Type III chondrules, as well as 1400 K and 1280 K residual condensates) (see Table S3). Carbonaceous chondrites and CAIs are not considered as they are both enriched in neutron-rich nuclides (^{48}Ca, ^{50}Ti, ^{54}Cr) relative to angrites (*e.g.*, Dauphas, 2017), which precludes a direct genetic link with the APB. For each 2-component mixture, between 0 and 100 % of the Fe was allowed to be removed into the core. A least-square minimization was then performed to find how closely the resulting hypothetical APB composition could be matched by some mixture between the average quenched Group 1 melt and its equilibrium olivine (*i.e.*, LEW 87051 and Olivine Fo 80.5).

The results of this exercise are presented in Fig. 12 (see also Supplementary Fig S2), as density maps of the residual between the hypothetical APB composition and the best fit using the quenched Group 1 compositions and equilibrium olivine. For each 2-component mixture, the composition that can be best reproduced by a mixture of primitive angritic melt + equilibrium olivine is given in Supplementary Table S4. We find that 2-component mixtures with AOAs produce generally poor fits (residual up to ~16 wt%), which makes sense as AOAs are too Ti rich and plot off the nebular trend in Fig. 10c. Furthermore, their low Fe content mainly precludes the formation of a core (see Supplementary Fig S2), which is an important feature to match. Both the high Ti and low Fe of AOAs testify to their very high temperature of formation, and suggest that the APB formed from material condensed at somewhat lower temperatures.

In contrast to AOAs, most 2-component mixtures involving the 1400 K and 1280 K first condensates provide decent fits (residuals below 1.91 wt%). In details, the closest fits are obtained when the 1400 K first condensates (Fig. 12) are considered as the high-T component, and mixtures involving enstatite or ordinary chondrites, Type IB chondrules and the 1280 K residual condensate all produce remarkable matches, with residuals below 1 wt% and r^2 values $\geq$ 0.9997 (Supplementary Table S4). The average of these specific 2-component mixtures is used to define the best estimate APB composition, and core size, from this minimization exercise.

Estimates of the bulk composition, mantle Fe/Si and core size derived using the various methods described above are summarized in Table 7. Collectively, these point to a conservative best estimate APB with Mg/Si of 1.29 ± 0.11, Al/Si of 0.117 ± 0.027, Ca/Si of 0.101 ± 0.025, Ti/Si of 0.0039 ± 0.0008, Fe/Si of 0.875 ± 0.185 and Cr/Si of 0.0062 ± 0.0038 (see Table 7 for oxide abundances, in wt%). The recommended core size thus obtained is 18 ± 6 wt% of the APB, in remarkable agreement with the 18 ± 11 % estimate from Steenstra et al. (2017), while the mantle Fe/Si ratio derived from the composition of primitive angritic melts (quenched Group 1) is 0.452 ± 0.089. To our knowledge, this is the first self-consistent estimate of the major elements composition of the APB.

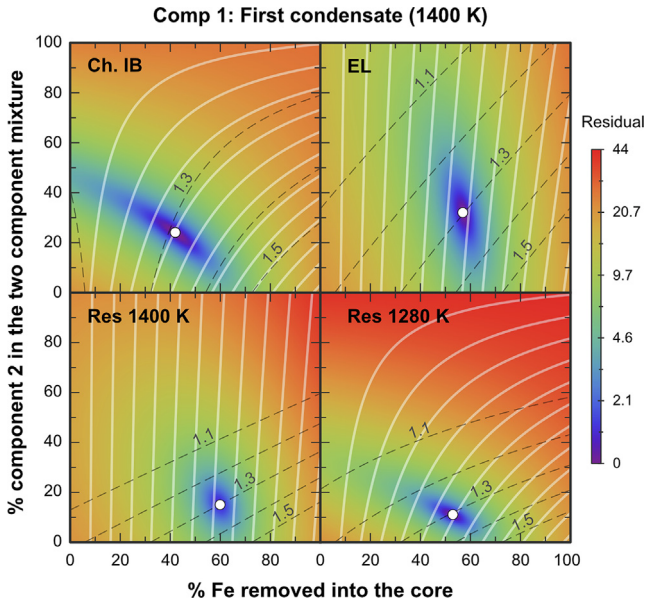

Fig. 12. Density maps showing the difference (*i.e.*, residual) between hypothetical APB compositions (2-component mixtures) and the best fit composition obtained by mixing a primitive angritic melt and its equilibrium olivine. For each panel, the x-axis denotes the amount of Fe sequestered into the core, and the y-axis the % of low-T component in the 2-component mixture. The high-T component is taken as the 1400 K first condensate (see Fig S2 in Supplementary Materials for maps using the 1280 K first condensate or AOAs instead). The low-T component is labeled in the top left corner of each panel. White curves are lines of equal core mass (by 3 % mass increment, from left to right). Dashed black curves are lines of equal Mg/Si ratio for the best fit composition obtained by mixing a primitive angritic melt and its equilibrium olivine (from 1.1 to 1.5, by 0.1 step increment). In each panel, the white circle denotes the optimal solution (*i.e.*, minimum residual), whose composition is reported in Table S4.

Notably, our estimate has a much higher Mg/Si and much lower Al/Si (as well as Ca/Si, and Ti/Si) than the one from Longhi (1999), who also derived an APB bulk composition based on 2-component mixing between chondrites from which metal had been removed (Allende- 40 % Fe) and some high-T component. The reason for this difference is that Longhi (1999) considered a high-T component formed at 1440 K, when only 10 % of the Mg and 15 % of the Si present in the nebula have condensed, while we considered a high-T component formed at 1400 K, when more than 70 % of the Mg and 50 % of the Si have condensed (Grossman, 1972). This small difference in temperature results in drastic changes in major element ratios in the total condensed material, and the resulting bulk composition of the APB. Additional experiments will be necessary to further test our proposed composition for the APB and its Mg-enriched nature.

5.4. Oxygen fugacity of the APB

We now discuss the constraints that our 1 atm and high-pressure experiments place on the fO_2 during crystallization of D'Orbigny-like angrites. Because our 1 atm experiments were performed over a range of redox conditions, we use the Mg# in the core of the clinopyroxene as an empirical tracer of fO_2 conditions. In Fig. 13, we plot the Mg# measured in the core of Cpx when they first appear in the 1 atm experimental charges as a function of fO_2 (filled circles). Because (i) Mg contents in the melt decrease as crystallization proceeds, and (ii) the Cpx appears slightly later in the crystallization sequence at lower fO_2 (Fig. 3), a negative trend is observed in Fig. 13. In natural angrites, pyroxenes in equilibrium with the most primitive melt(s) will have the highest core Mg#.

Table 7
APB bulk composition best estimates (atomic ratios).

Method		APB bulk composition						APB mantle	APB core (wt%)
		Mg/Si	Al/Si	Ca/Si	Ti/Si	Fe/Si	Cr/Si	Fe/Si	
Intercept nebular trend & Ol-melt tie lines[a]		1.18–1.40	0.107–0.144	0.089–0.125	0.0031–0.0046	0.95–1.04	0.005–0.010	0.363–0.541	16–24
Two-component mixtures[b]		1.29–1.31	0.109–0.114	0.076–0.080	0.0031–0.0033	0.69–1.06	0–0.0052	0.400–0.404	12–24
Ol-melt best fit to 2-component mixtures[c]		1.29–1.31	0.090–0.094	0.093–0.097	0.0037–0.0038	N/A	0.0024–0.0024	0.403–0.403	N/A
Recommended value[d]		**1.29 ± 0.11**	**0.117 ± 0.027**	**0.101 ± 0.025**	**0.0039 ± 0.0008**	**0.875 ± 0.185**	**0.0062 ± 0.0038**	**0.452 ± 0.089**	**18 ± 6**
Equivalent in oxide weight %	SiO_2	MgO	Al_2O_3	CaO	TiO_2	FeO	Cr_2O_3		
Recommended value APB[d]	**32.07**	**27.76**	**3.18**	**3.01**	**0.16**	**33.56**	**0.25**		
Recommended value bulk silicate angrite[d]	**38.29**	**33.13**	**3.80**	**3.59**	**0.20**		**0.30**	**20.69**	

[a] Assumes the APB falls on the nebular trend defined by chondrites (grey envelop in Fig. 10), except for Fe/Si and Cr/Si ratios, which are predicted by projecting the Mg/Si ratio of 1.18 to 1.40 onto the tie-line between the first (1400 K) and residual condensates (1400–830 K) from Morbidelli et al. (2020) (purple points in Fig. 11).
[b] Average APB composition and core size derived from 2 end-member mixing calculations with $r^2 \geq 0.9997$ and residuals ≤ 1.1 (Table S4).
[c] Best fit to the 2-component mixture produced by mixing the primitive angrite melt composition (LEW 87051) and its corresponding equilibrium olivine (Fo 80.5).
[d] Full range from the three estimates, except for Cr/Si where the 0 value is omitted (as angrites clearly contain Cr).

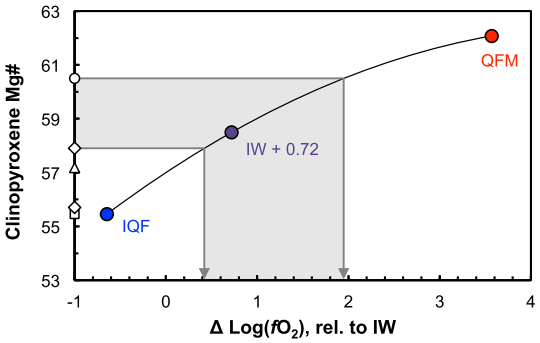

Fig. 13. Mg# in the core of clinopyroxene as function of oxygen fugacity (log units, relative to the IW buffer). Filled circles represent the values measured in the 1 atm experimental charges (this study). Open symbols on the y-axis denote Mg# measured in natural specimens of quenched Group 2 angrites: the diamonds, square and circle are data from D'Orbigny reported in, respectively, Mittlefehldt et al., (2002), Kurat et al., (2004), and Floss et al., (2003), and the triangle shows data from NWA 1296 (Jambon et al., 2005). The highest Mg# record the fO_2 relevant to the crystallization of the primitive basaltic angrite melts, at ~IW+0.4 to IW+2.

Previous studies have reported high Mg# in the cores of Cpx from natural quenched Group 2 angrites, with values typically between 55.5 and 57.9 in D'Orbigny and NWA 1296 (Mittlefehldt et al., 2002; Kurat et al., 2004; Jambon et al., 2005), and the highest value of 60.5 measured in D'Orbigny (Floss et al., 2003). Based on the trend defined by our 1 atm experiments, these values indicate crystallization from a melt under fO_2 conditions as oxidizing as ~IW+0.4 to IW+2 (Fig. 13).

On the other hand, some of our high-pressure experiments provide constraints on the fO_2 relevant to the source magma of quenched angrites. Indeed, at 8 kbar (B1402 and B1403; Table 4) we obtain multi-saturation surfaces that match the mineralogy of quenched Group 2 angrites (Table 5). The fO_2 of these experiments is ~IW+1.2, a value consistent with those derived from our 1 atm experiments. Such oxidizing conditions are in excellent agreement with previous independent estimates of fO_2 during the crystallization of both quenched and plutonic angrites, which collectively point to values between ~IW-0.7 and IW+2 (Table 8).

Reconciling these oxidizing conditions with the differentiation of a core on the APB – as evidenced by paleomagnetic data

Table 8
Oxygen fugacity estimates for the Angrite Parent Body.

Meteorite	Type	Method	ΔIW	Refs.
During magma crystallization				
AdoR	Plut.	Intrinsic fO_2 measurements using the solid-electrolyte oxygen cell method.	0 to +1.2	[1]
AdoR	Plut.	Dynamic crystallization experiments.	~ 0 to >0	[2]
LEW 86010	Plut.	Comparison of experimental Eu/Gd partition coefficients in plagioclase and pyroxene with natural values.	~ +0.8	[3]
NWA 2999	Plut.	Comparison of experimental Eu/Gd partition coefficients in plagioclase and pyroxene with natural values.	+0.5 to +1.1	[4]
NWA 4590	Plut.	Comparison of experimental Eu/Gd partition coefficients in plagioclase and pyroxene with natural values.	+1.0 to +2.4	[4]
NWA 4801	Plut.	Comparison of experimental Eu/Gd partition coefficients in plagioclase and pyroxene with natural values.	+1.0 to +1.7	[4]
LEW 87051	Volc.	K-edge XANES determination of chromium valence (Cr^{2+}/Cr_{Total}) in olivine crystals.	~ 0 to +2 (core to rim)	[5]
D'Orbigny	Volc.	Partial melting experiments of CV chondrites to reproduce the bulk composition of D'Orbigny.	+1 to +2	[6–8]
D'Orbigny	Volc.	XANES determination of vanadium valence in clinopyroxene crystals.	−0.7 to +0.5 (core to rim)	[9]
D'Orbigny	Volc.	Comparison of Mg# in Cpx cores in 1 atm equilibrium experiments and natural D'Orbigny-like angrites.	+0.4 to +2.0	This work
During core formation				
Bulk silicate APB		Comparison of experimentally determined metal-silicate partition coefficient of moderately siderophile elements with values required to explain their depletion in the APB mantle relative to a CV bulk composition. See set of elements used in the footnotes.	~ −1[a]	[10]
Bulk silicate APB			~ −1[b]	[11]
Bulk silicate APB			−1.40 ± 0.45[c]	[12]

References: [1] Brett et al., 1977; [2] Lofgren & Lanier, 1992; [3] McKay et al., 1994; [4] Sanborn & Wadhwa, 2021; [5] Shearer et al., 2016; [6–8] Jurewicz et al., 1991, 1993, 2004; [9] King et al., 2012; [10] Righter, 2008; [11] Shirai et al., 2009b; [12] Steenstra et al., 2017.
[a] Using Co, Ni and W abundances, assuming equilibrium between a peridotite mantle and C-bearing FeNi metallic liquid core (8 mass %) at 2173 K and 5 kbar.
[b] Same as 'a' but with the addition of Mo abundances, and at 2073 K and 1 kbar.
[c] Using Co, Ni, Ga, Mo, and W abundances, for a range of core compositions, sizes, and temperatures, at 1 kbar.

(Weiss et al., 2008), W isotope systematics (Markowski et al., 2007; Kleine et al., 2009, 2012), and the depletions of siderophile elements relative to chondrites (Righter, 2008; Shirai et al., 2009b; Riches et al., 2012; Steenstra et al., 2017) – is a well-known conundrum. Indeed, under conditions as oxidizing as IW+1 or +2, Fe metal is, by definition, unstable, which would prevent core formation from taking place. At the same time, the metal-silicate partition coefficient of siderophile elements decreases with increasing fO_2, which would require a large (~60 % by mass) core to explain the siderophile element depletion in the APB mantle (Righter, 2008). Because (i) core formation on the APB did happen, and (ii) formation of a large core under oxidizing conditions is highly unlikely, previous studies have proposed that the APB formed and differentiated a core under mildly reducing conditions (~IW-1.4 ± 0.5, Table 8), so as to explain the siderophile element depletion in the APB mantle. This scenario requires that the higher fO_2 conditions during crystallization recorded in angrite specimens testify to either (i) a subsequent oxidation of the APB mantle, or (ii) oxidation of the basaltic angrite melts upon degassing and eruption (Righter, 2008; Shirai et al., 2009b). The latter would be consistent with the presence of vesicles in some quenched angrites (McCoy et al., 2006).

Our data, pointing to relatively oxidized conditions during crystallization of D'Orbigny-like angrites, further strengthen the conclusion that a change in fO_2 occurred on the APB between core formation, at ~IW-1.4 ± 0.5, and magma crystallization, at ~IW+1 ± 1. Sanborn and Wadhwa (2021) observed that this change could be related to the addition of water/volatiles to the APB during this time interval (Sarafian et al., 2017a, 2017b).

5.5. Minimum size of the APB

Since the APB is currently unknown (*i.e.*, has not been observed), its size can only be constrained indirectly. While it is clear that the APB must have been larger than 100 km in radius, or else angrite melts would have been lost to space during eruption, and no basaltic plutonic or quenched angrites would be observed (Wilson and Keil, 1991), accurately estimating the size of the APB remains an important point of debate (*e.g.*, Scott and Bottke, 2011; Keil, 2012). Traditionally, the APB has been assumed to be a small body, similar in size to asteroid 4 Vesta (r ~ 260 km), the presumed parent body of HED meteorites. Multiple lines of evidence, however, support the idea of a larger APB. For instance, the presence of solar-like gases trapped in D'Orbigny glass is consistent with a parent body large enough to retain a nebular atmosphere (Busemann et al., 2006). Furthermore, the large and uniform spread in cosmic-ray exposure ages in angrites (~0.6–60 Ma) points to an APB large enough for prolonged impact/ejection events (Nakashima et al., 2018). Metamorphic coronas in NWA 3164 point to contact metamorphism on the APB, at P conditions < 9 kbar, suggesting that the APB must have been a large asteroid or a planetary-size body (Baghdadi et al., 2013). Quantitatively, estimates on the size of the APB have recently been proposed based on (i) the volatile (H, C) content of melt inclusions within angrite specimens, which point to an APB radius of at least 270 km, and probably ≥ 340 km (Sarafian et al., 2017a), and (ii) the presence of a sustained core dynamo on the APB up to 11 Myr after CAI formation (Weiss et al., 2008; Wang et al., 2017), whose paleointensity combined with chronometric data and thermal modelling indicate a rapid accretion to a minimum APB radius of 420 km only 1.8 Myr after CAI formation (Bryson et al., 2019; Dodds et al., 2021).

Our pressure experiments indicate that a pressure of 6 to 9 kbar is necessary for multiple saturation in Ol + Cpx + Sp (±Plag) in the source magma of quenched Group 2 angrites (Fig. 6), which allows us to independently determine a lower limit on the size of the APB. Assuming a spherical APB under hydrostatic conditions (*i.e.*, the only force at play is the APB gravitational force), the pressure profile inside the APB can be calculated as:

$$P(z) = \int_0^z \rho(z) g(z) dz \quad (1)$$

where z is depth (downward from the surface), $\rho(z)$ is the density at depth z (in kg/m^3), and $g(z)$ is the acceleration of gravity at depth z (in m/s^2), defined as:

$$g(z) = -\frac{G \times M(z)}{(R_{APB} - z)^2} \quad (2)$$

In Eq. (2), G is the gravitational constant (6.674×10^{-11}N.m^2/kg^2), $M(z)$ is the mass of the APB material below depth z, and $(R_{APB} - z)$ is the distance between the center of the APB and depth z. For a given density profile, $M(z)$ can be easily calculated, yielding through Eq. (2) and (1), the depth profiles for the local gravity and pressure in the APB.

Fig. 14 shows the APB pressure profiles calculated (see code in Supplementary Materials) for three scenarii: a pure silicate APB (*i.e.*, no core) of constant density, $\rho_{silicate}$ = 3300 kg/m^3 (Fig. 14a), an APB with a 14 wt% core composed of 80 % Fe and 20 % Ni, ρ_{core} = 8080 kg/m^3 (Fig. 14b), and an APB with a 21 wt% core composed of 70 % Fe, 20 % Ni, 5 % S, and 5 % C, ρ_{core} = 7500 kg/m^3 (Fig. 14c). The core masses and compositions are taken from Steenstra et al. (2017). While the core compositions simply illustrate possible compositions assuming a volatile-poor (only Fe-Ni) and volatile-rich (with significant C and S) APB, the corresponding core masses are the ones that best explain the metal depletion in the APB mantle based on metal-silicate partition coefficients (from Steenstra et al. 2017). To reach a pressure of 6 kbar in the silicate portion of the APB translates to a minimum APB radius of ~594–628 km, while a pressure of 9 kbar requires a radius of ~728–769 km (Fig. 14, red envelopes). The presence, size and compositions of the APB core have little influence on these values, as the higher density of the metallic core results in a higher local acceleration of gravity (and thus a higher pressure) at lower depth compared to a pure silicate APB.

The above lower limits are fully compatible with the minimum radii of 270 km (Sarafian et al., 2017a) and 420 km (Bryson et al., 2019; Dodds et al., 2021) based on volatile content and paleomagnetic field intensities of angrites and their melt inclusions, but imply a significantly larger APB than previously thought. Indeed, the ~600 to 770 km estimates shown in Fig. 14 (red envelopes) are very conservative lower limits, as they assume that the parental magma of angrites formed in a source located in the deepest silicate portion of the APB (near the center of the APB in the core-free case, or otherwise at the core-mantle boundary). Under these conditions, the extraction and eruption of such melts onto the surface of the APB would be physically hard to explain. For the angrite parental melt to be able to equilibrate at ~6–9 kbar before eruption and quenching at or near the surface, therefore requires that the APB was much larger than the lower limit of ~600 to 770 km derived above.

Assuming D'Orbigny and other quenched Group 2 angrites are evolved lavas derived from a parental magma with quenched Group 1 composition (*e.g.*, Asuka 881371, LEW 87051, NWA 7812), a first-order estimate on the pressure at which these parental melts were formed can be obtained by identifying the conditions under which their bulk compositions are saturated with multiple phases on the liquidus. The parameterization of Grove et al. (2013) yields pressures between 26 and 32 kbar. Similar values are obtained using the Perple_X model (Connolly, 2009) with the Holland et al. (2018) database (23 to 31 kbar, accounting for a small pressure correction based on Barr and Grove (2013) exper-

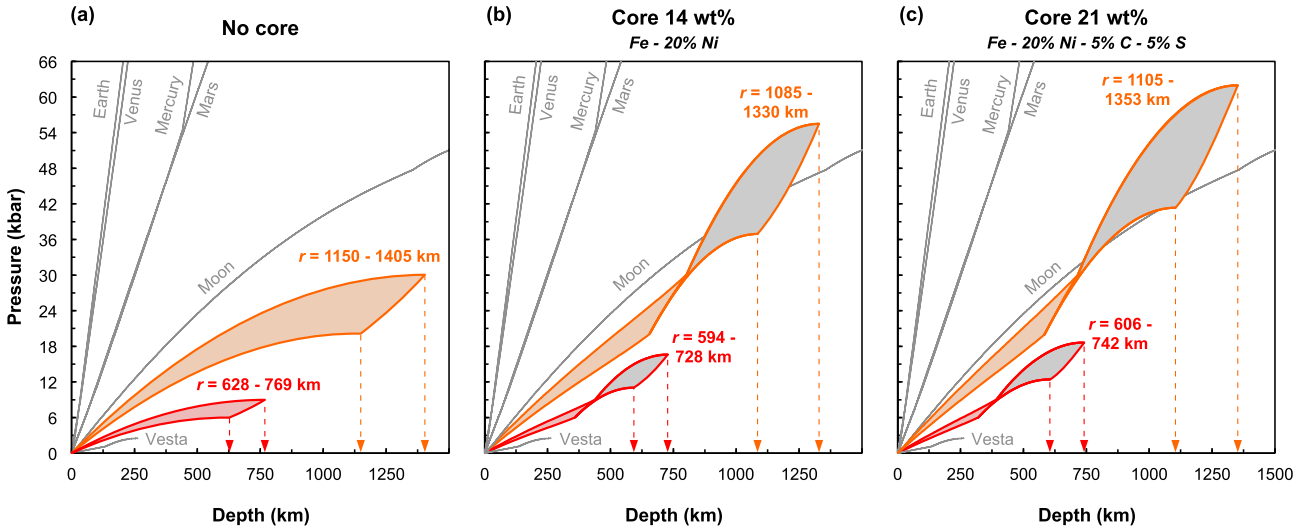

Fig. 14. Hydrostatic pressure as a function of depth. Pressure profiles in hypothetical APBs are shown for (a) a core-free APB, (b) an APB with a 14 wt% by mass core, made of Fe-Ni (80:20), and (c) an APB with a 21 wt% by mass core, made of Fe-Ni-C-S (70:20:5:5). For the APB profiles, a grey filling denotes the core. Red (orange) envelopes are bound by the profiles of the smallest APBs reaching the 6 and 9 kbar (20 and 30kbar) threshold in the APB mantle. These constraints from quenched Group 2 (and Group 1) angrites point to a minimum radius of ~600–770 km (~1085–1405 km) for the APB, regardless of the presence, size and composition of a core. Profiles for the telluric planets, as well as the Moon and Vesta are also shown, and were calculated using literature density profiles: Mercury after Rivoldini et al. (2009), Venus after Aitta (2012), Earth after PREM, http://ds.iris.edu/ds/products/emc-prem/, Dziewonski and Anderson (1981), Mars after Bertka and Fei (1998) assuming at core with 14 wt% S (Dreibus and Wanke, 1985), Moon after the seismic VPREMOON model from Garcia et al. (2011, 2012); and Vesta after Ruzicka et al. (1997).

iments, see Supplementary Material), or the PETROGEN model (24–29 kbar, Krein et al., 2020). While additional experiments would allow to constrain more precisely the pressure of the source of Group 1 angrites, the convergence of independent models is informative and indicate that the APB must have been large enough for pressures of ~20–30 kbar to be reached in the source region of quenched angrites. This translates to an APB radius of at least 1085–1405 km (Fig. 14, orange envelopes).

In summary (Fig. 15), our pressure experiments indicate that the APB had a radius of at least ~600–770 km (about 3 times larger than Vesta, the parent body of HED meteorites). When the fractional crystallization relationship between the two groups of quenched angrites is considered, this lower limit is increased to ~1085–1405 km, raising the possibility of a Moon-sized (if not larger) APB. The latter would naturally explain the relatively elevated abundance of Highly Siderophile Element (HSE) in the angritic mantle (10 ng/g), which has been proposed to be controlled by the parent-body size (Dale et al., 2012). In Fig. 16, we show that the 9 and 30 kbar lower limits derived above confirm that the APB plots on the HSE content vs parent body mass trend defined by Earth, Mars and Vesta, and point to an APB mass of $\sim 10^{26}$ g.

5.6. Where is the APB?

The rare asteroids with reflectance spectra matching those of angrites are small (r < 34 km, McCord et al., 1970; Burbine et al., 2001; Rivkin et al., 2007), which implies that the APB either (i) has not been observed yet, (ii) was extremely small, or (iii) got disrupted or destroyed early in its history (Scott and Bottke, 2011). The large size of the APB inferred from our experiments supports

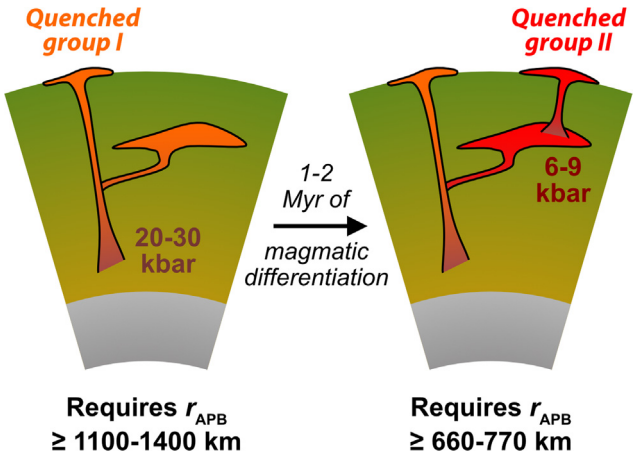

Fig. 15. Illustration of the temporal and compositional relationship between quenched Group 1 and Group 2 angrites. The values in kbar denote the pressure of multiple saturation derived from our high-pressure experiments (Group 2 angrites) and modeling (Group 1). The minimum APB radii implied by these pressures are also shown.

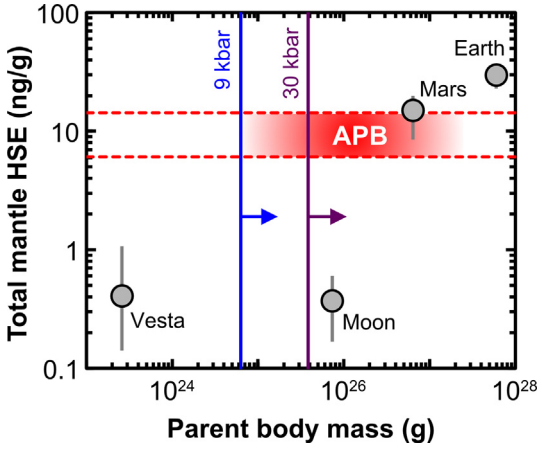

Fig. 16. Total mantle HSE concentration plotted against parent body mass for the Earth, Mars, Moon and Vesta (data from Dale et al., 2012). The range of HSE concentration in the APB mantle is shown as horizontal red dotted lines (Dale et al., 2012), while the constraints on the minimum APB size (this work) are shown as vertical lines. The lower limits of 9 and 30 kbar derived in Section 5.5 confirm that the APB plots on the trend defined by Earth, Mars and Vesta, and point to a Moon-sized (if not larger) APB.

the proposal that the APB was a major body in the early inner Solar System (Baghdadi et al., 2013; Sarafian et al., 2017a; Bryson et al., 2019; Dodds et al., 2021), and thus favors the latter hypothesis. Based on elemental and isotopic mass balance considerations, Fitoussi et al. (2016) even proposed that the APB (or an APB-like material) was a major building block of the terrestrial planets, that could account for up to 50–60 % of Earth's and Mars' mass, with the remainder mass coming from ordinary chondrites (~30 %) and CI/CV carbonaceous chondrites (~10–20 %). Using a similar approach, but not limiting the number of possible components to four, Liebske and Khan (2019) found a smaller but still significant APB contribution to Earth/Mars.

The idea that the APB was accreted into one (or several) of the terrestrial planets is consistent with models of terrestrial planet formation by collision between early formed planetary embryos from the inner Solar System (*e.g.*, Chambers and Wetherill, 1998). The status of the APB as a true planetary embryo is supported by (i) the early accretion (~0.5 to 1 Myr after CAIs) and differentiation (within ~2 Myr after CAI formation) of the APB (Markowski et al., 2007; Kleine et al., 2009, 2012), (ii) the very old crystallization ages of angrites, ranging from 4 to 11 Myr after CAIs (see Tissot et al., 2017 and references therein), and (iii) the reduced and volatile-depleted nature of the APB, as well as its non-carbonaceous isotope composition (Budde et al., 2019), which both suggest a formation in the inner Solar System. The large size and bulk APB composition derived in this study, consistent with a nebular origin at relatively high temperatures (~1300–1400 K), further strengthen the case that the APB was indeed a planetary embryo. As such, it seems most likely that the APB was disrupted early in the history of the Solar System and accreted into the terrestrial planets.

6. Conclusions

Taking advantage of the rapidly growing number of known angrite meteorites (which has more than quintupled in 20 years), we attempted here to revisit their petrogenesis and place novel constraints on key features of the APB. We found that quenched (*i.e.*, volcanic) specimens define two distinct compositional groups: Group 1, which currently includes Asuka 881371, LEW 87051, NWA 1670, NWA 5167, NWA 7812 and NWA 12774, and Group 2, which currently includes D'Orbigny, Sahara 99555 and NWA 1296 (Fig. 1). We showed that these two groups can be readily related by fractional crystallization (Fig. 7), with Group 1 specimens representing more primitive angritic melts, and Group 2 specimens representing more evolved lavas, whose composition sits on an Ol + Cpx + Sp (±Plag at low pressure) multiple saturation boundary.

Recognizing that quenched Group 1 specimens likely capture the composition of primitive angritic melts, we derived a self-consistent estimate of the major elements abundances in the APB (Table 7), which suggests that the refractory-enriched (and volatile-depleted) nature of the APB is a primitive feature resulting from nebular fractionation at high-T (~1300–1400 K), rather than the result of parent body processing. Importantly, our APB bulk composition estimate matches the proposed Mg/Si ratio of 1.3 derived from the angrite δ^{30}Si values, and yields a core size (18 ± 6 wt%) in agreement with the siderophile elements depletion in the APB mantle.

Through a series of 1 atm and high-pressure crystallization experiments, we established the liquid phase equilibria of angrites (Fig. 6). Our data indicate that crystallization of D'Orbigny-like (Group 2) angrites occurred under relatively oxidized conditions (~IW+1 ± 1), in contrast with the more reducing conditions (IW-1.4 ± 0.5) thought to prevail during core formation, implying a change in fO_2 in the APB over its evolution. Furthermore, our results place a stringent lower limit on the size of the APB, whose radius must have been at least ~600–770 km (3 times larger than Vesta), and more likely greater than 1085–1405 km, raising the possibility of a Moon-sized APB (Figs. 14-15).

When combined with its extremely early accretion (~0.5–1 Myr after CAIs) and differentiation (within 2 Myr after CAIs), the large size and refractory-enriched nature of the APB (this work) suggests that it was an important body in the inner Early Solar System. In fact, in light of the above observations, we propose that the APB represents the archetype of the first-generation of refractory-enriched planetesimals and embryos formed in the *innermost* part of the inner Solar System (<1 AU), and which accreted in the telluric planets. In this framework, the terrestrial planets would grow dry (*i.e.*, devoid of volatiles), at least during the early stages of their accretion, and their volatile inventory would be delivered later in their history, through accretion of more volatile rich materials, such as chondrites and/or comets.

Declaration of Competing Interest

The authors declare that they have no known competing financial interests or personal relationships that could have appeared to influence the work reported in this paper.

Data availability

All data is available in the Supplementary Materials or upon request.

Acknowledgments

Nilanjan Chatterjee's maintenance of, and help with, the EMPA is gratefully acknowledged. This work was supported by a W.O. Crosby Postdoctoral Fellowship from MIT, NSF grants EAR-1824002 and MGG-2054892, a Packard Fellowship, a research award from the Heritage Medical Research Institute, and start-up funds (provided by Caltech) to FLHT. MC was funded by a NASA Emerging Worlds grant (NNX16AD29J) at MIT (to TLG) and DFG grant TRR-170 at DLR. This is TRR-170 contribution #177. We thank Paul C. Buchanan, Aaron S. Bell, and one anonymous reviewer for constructive reviews that helped improve the manuscript, and editor Audrey Bouvier for prompt and careful editorial handling.

Appendix A. Supplementary material

Supplementary material to this article can be found online at https://doi.org/10.1016/j.gca.2022.09.031.

References

Aitta, A., 2012. Venus' internal structure, temperature and core composition. Icarus 218, 967–974.
Amelin, Y., 2008. U-Pb ages of angrites. Geochim. Cosmochim. Acta 72, 221–232.
Amelin, Y., Irving, A.J., 2007. Seven Million Years of Evolution on the Angrite Parent Body from Pb-Isotopic Data. In *Chronology of Meteorites and the Early Solar System*., 20–21
Armstrong, J.T., 1995. Citzaf-a package of correction programs for the quantitative Electron Microbeam X-Ray-Analysis of thick polished materials, thin-films, and particles. Microbeam Anal. 4, 177–200.
Asplund, M., Grevesse, N., Sauval, A.J., Scott, P., 2009. The Chemical Composition of the Sun. Ann. Rev. Astron. Astrophys. 47, 481–522.
Baghdadi, B., Godard, G., Jambon, A., 2013. Evolution of the angrite parent body: Implications of metamorphic coronas in NWA 3164. Meteorit. Planet. Sci. 48, 1873–1893.
Baghdadi, B., Jambon, A., Barrat, J.-A., 2015. Metamorphic angrite Northwest Africa 3164/5167 compared to magmatic angrites. Geochim. Cosmochim. Acta 168, 1–21.

Barr, J.A., Grove, T.L., 2013. Experimental petrology of the Apollo 15 group A green glasses: Melting primordial lunar mantle and magma ocean cumulate assimilation. Geochim. Cosmochim. Acta 106, 216–230.
Berndt, J., Liebske, C., Holtz, F., Freise, M., Nowak, M., Ziegenbein, D., Hurkuck, W., Koepke, J., 2002. A combined rapid-quench and H_2 -membrane setup for internally heated pressure vessels: Description and application for water solubility in basaltic melts. Am. Mineral. 87, 1717–1726.
Bertka, C.M., Fei, Y., 1998. Density profile of an SNC model Martian interior and the moment-of-inertia factor of Mars. Earth Planet. Sci. Lett. 157, 79–88.
Blundy, J., Melekhova, E., Ziberna, L., Humphreys, M.C.S., Cerantola, V., Brooker, R.A., McCammon, C.A., Pichavant, M., Ulmer, P., 2020. Effect of redox on Fe–Mg–Mn exchange between olivine and melt and an oxybarometer for basalts. Contrib. Miner. Petrol. 175, 103.
Boyd, F.R., England, J.L., 1960. Apparatus for phase-equilibrium measurements at pressures up to 50 kilobars and temperatures up to 1750°C. J. Geophys. Res. 65, 741–748.
Brett, R., Huebner, J.S., Sato, M., 1977. Measured oxygen fugacities of the Angra dos Reis achondrite as a function of temperature. Earth Planet. Sci. Lett. 35, 363–368.
Bryson, J.F.J., Neufeld, J.A., Nimmo, F., 2019. Constraints on asteroid magnetic field evolution and the radii of meteorite parent bodies from thermal modelling. Earth Planet. Sci. Lett. 521, 68–78.
Budde, G., Burkhardt, C., Kleine, T., 2019. Molybdenum isotopic evidence for the late accretion of outer Solar System material to Earth. Nat. Astron 3, 736–741.
Burbine, T.H., McCoy, T.J., Binzel, R.P., 2001. Spectra of angrites and possible parent bodies. In: In *Lunar and Planetary Science Conference*, p. 1857.
Busemann, H., Lorenzetti, S., Eugster, O., 2006. Noble gases in D'Orbigny, Sahara 99555 and D'Orbigny glass—Evidence for early planetary processing on the angrite parent body. Geochim. Cosmochim. Acta 70, 5403–5425.
Chambers, J.E., Wetherill, G.W., 1998. Making the Terrestrial Planets: N-Body Integrations of Planetary Embryos in Three Dimensions. Icarus 136, 304–327.
Charlier, B.L.A., Parkinson, I.J., Burton, K.W., Grady, M.M., Wilson, C.J.N., Smith, E.G. C., 2017. Stable strontium isotopic heterogeneity in the solar system from double-spike data. Geochemical Perspective Letters, 35–40.
Collinet, M., Grove, T.L., 2020. Formation of primitive achondrites by partial melting of alkali-undepleted planetesimals in the inner solar system. Geochim. Cosmochim. Acta 277, 358–376.
Connolly, J.A.D., 2009. The geodynamic equation of state: What and how. Geochem. Geophys. Geosyst. 10, n/a-n/a.
Crozaz, G., McKay, G., 1990. Rare earth elements in Angra dos Reis and Lewis Cliff 86010, two meteorites with similar but distinct magma evolutions. Earth Planet. Sci. Lett. 97, 369–381.
Dale, C.W., Burton, K.W., Greenwood, R.C., Gannoun, A., Wade, J., Wood, B.J., Pearson, D.G., 2012. Late Accretion on the Earliest Planetesimals Revealed by the Highly Siderophile Elements. Science 336, 72–75.
Dauphas, N., 2017. The isotopic nature of the Earth's accreting material through time. Nature 541, 521–524.
Dauphas, N., Poitrasson, F., Burkhardt, C., Kobayashi, H., Kurosawa, K., 2015. Planetary and meteoritic Mg/Si and δ 30 Si variations inherited from solar nebula chemistry. Earth Planet. Sci. Lett. 427, 236–248.
Dauphas, N., Nie, N.X., Blanchard, M., Zhang, Z.J., Zeng, H., Hu, J.Y., Meheut, M., Visscher, C., Canup, R., Hopp, T., 2022. The Extent, Nature, and Origin of K and Rb Depletions and Isotopic Fractionations in Earth, the Moon, and Other Planetary Bodies. The Planetary Science Journal 3, 29.
Delaney, J.S., Sutton, S.R., 1988. Lewis Cliff 86010, an ADORable Antarctican. In *Lunar and Planetary Science Conference*, 265–266.
Dodds, K.H., Bryson, J.F.J., Neufeld, J.A., Harrison, R.J., 2021. The Thermal Evolution of Planetesimals During Accretion and Differentiation: Consequences for Dynamo Generation by Thermally-Driven Convection. J. Geophys. Res. Planets 126.
Dreibus, G., Wanke, H., 1985. Mars, a volatile-rich planet. Meteoritics 20, 367–381.
Dziewonski, A.M., Anderson, D.L., 1981. Preliminary reference Earth model. Phys. Earth Planet. Inter. 25, 297–356.
Fitoussi, C., Bourdon, B., Wang, X., 2016. The building blocks of Earth and Mars: A close genetic link. Earth Planet. Sci. Lett. 434, 151–160.
Fittipaldo, M.M., Jones, R.H., Shearer, C.K., 2005. Thermal histories of angrite meteorites: Trace element partitioning among silicate minerals in Angra dos Reis, Lewis Cliff 86010, and experimental analogs. Meteorit. Planet. Sci. 40, 573–589.
Floss, C., Crozaz, G., McKay, G., Mikouchi, T., Killgore, M., 2003. Petrogenesis of angrites. Geochim. Cosmochim. Acta 67, 4775–4789.
Garcia, R.F., Gagnepain-Beyneix, J., Chevrot, S., Lognonné, P., 2011. Very preliminary reference Moon model. Phys. Earth Planet. Inter. 188, 96–113.
Garcia, R.F., Gagnepain-Beyneix, J., Chevrot, S., Lognonné, P., 2012. Erratum to "Very Preliminary Reference Moon Model", by R.F. Garcia, J. Gagnepain-Beyneix, S. Chevrot, P. Lognonné [Phys. Earth Planet. Inter. 188 (2011) 96–113]. Phys. Earth Planet. Inter. 202–203, 89–91.
Gellissen, M., Palme, H., Korotev, R.L., Irving, A.J., 2007. NWA 2999, A Unique Angrite with a Large Chondritic Component. In: In *Lunar and Planetary Science Conference*, p. 1612.
Grossman, L., 1972. Condensation in the primitive solar nebula. Geochim. Cosmochim. Acta 36, 597–619.
Grove, T.L., 1982. Use of FePt alloys to eliminate the iron loss problem in 1 atmosphere gas mixing experiments: Theoretical and practical considerations. Contrib. Miner. Petrol. 78, 298–304.
Grove, T.L., Bence, A., 1977. Experimental study of pyroxene-liquid interaction in quartz-normative basalt 15597. In *Lunar and Planetary Science Conference Proceedings*, 1549–1579.
Grove, T.L., Bryan, W.B., 1983. Fractionation of pyroxene-phyric MORB at low pressure: An experimental study. Contrib. Miner. Petrol. 84, 293–309.
Grove, T.L., Kinzler, R.J., Bryan, W.B., 1992. Fractionation of Mid-Ocean Ridge Basalt (MORB). In: Morgan, J.P., Blackman, D.K., Sinton, J.M. (Eds.), Geophysical Monograph Series. American Geophysical Union, Washington, D. C., pp. 281–310.
Grove, T.L., Holbig, E.S., Barr, J.A., Till, C.B., Krawczynski, M.J., 2013. Melts of garnet lherzolite: experiments, models and comparison to melts of pyroxenite and carbonated lherzolite. Contrib. Miner. Petrol. 166, 887–910.
Halliday, A.N., Porcelli, D., 2001. In search of lost planets – the paleocosmochemistry of the inner solar system. Earth Planet. Sci. Lett. 192, 545–559.
Hays, J.F., 1966. Lime-alumina-silica. *Carnegie Inst Wash Yearb* 65, 234–239.
Hezel, D.C., Palme, H., Brenker, F.E., Nasdala, L., 2003. Evidence for fractional condensation and reprocessing at high temperatures in CH chondrites. Meteorit. Planet. Sci. 38, 1199–1215.
Holland, T.J.B., Green, E.C.R., Powell, R., 2018. Melting of Peridotites through to Granites: A Simple Thermodynamic Model in the System KNCFMASHTOCr. J. Petrol. 59, 881–900.
Huebner, J.S., 1971. Buffering Techniques for Hydrostatic Systems at Elevated Pressures. In: Ulmer, G.C. (Ed.), Research Techniques for High Pressure and High Temperature. Springer, Berlin Heidelberg, Berlin, Heidelberg, pp. 123–177.
Irving, A.J., Kuehner, S.M., Chen, G., Conrey, R.M., Ziegler, K., Pitt, D., 2013. Petrologic, Elemental and Oxygen Isotopic Characterization of Mg-Rich, Olivine-Phyric Quenched Angrite Northwest Africa 7812. Meteorit. Planet. Sci. 48, A182–A.
Irving, A.J., Kuehner, S., Righter, M., Pitt, D., Tutolo, B.M., Evans, B.W., 2019. Petrologic, elemental, isotopic and magnetic characterization of vesicular hypabyssal angrites Northwest Africa 12004 and Northwest Africa 12320. In: In *Lunar and Planetary Science Conference*, p. 2758.
Irving, A.J., Carpenter, P.K., Tepper, J.H., Righter, M., Lapen, T.J., Busemann, H., 2020. Petrology and Chemical Composition of Olivine-Pyroxene-Phyric Quenched Angrite Northwest Africa 12774. In: In *Lunar and Planetary Science Conference*, p. 2399.
Jakobsson, S., Oskarsson, N., 1994. The system C-O in equilibrium with graphite at high pressure and temperature: An experimental study. Geochim. Cosmochim. Acta 58, 9–17.
Jambon, A., Barrat, J.A., Boudouma, O., Fonteilles, M., Badia, D., Göpel, C., Bohn, M., 2005. Mineralogy and petrology of the angrite Northwest Africa 1296. Meteorit. Planet. Sci. 40, 361–375.
Jambon, A., Boudouma, O., Fonteilles, M., Guillou, C.L., Badia, D., Barrat, J.-A., 2008. Petrology and mineralogy of the angrite Northwest Africa 1670. Meteorit. Planet. Sci. 43, 1783–1795.
Jurewicz, A., Jones, J., Mittlefehldt, D., Longhi, J., 2004. Devolatilized-Allende partial melts as an analog for primitive angrite magmas. In: In *Lunar and Planetary Science Conference*, p. 1417.
Jurewicz, A.J.G., Mittlefehldt, D.W., Jones, J.H., 1991. Partial Melting of the Allende (Cv3) Meteorite - Implications for Origins of Basaltic Meteorites. Science 252, 695–698.
Jurewicz, A.J.G., Mittlefehldt, D.W., Jones, J.H., 1993. Experimental Partial Melting of the Allende (Cv) and Murchison (Cm) Chondrites and the Origin of Asteroidal Basalts. Geochim. Cosmochim. Acta 57, 2123–2139.
Jurewicz, A.J.G., Mittlefehldt, D.W., Jones, J.H., 1995. Experimental partial melting of the St. Severin (LL) and Lost City (H) chondrites. Geochim. Cosmochim. Acta 59, 391–408.
Keil, K., 2012. Angrites, a small but diverse suite of ancient, silica-undersaturated volcanic-plutonic mafic meteorites, and the history of their parent asteroid. Geochemistry 72, 191–218.
King, P.L., Spilde, M.N., Wirick, S., Lanzirotti, A., Agee, C.B., 2012. Redox history of early solar system planetesimals recorded in the D'Orbigny angrite (abstract# 1659). In: In *Lunar and Planetary Science Conference*, p. 2436.
Kleine, T., Touboul, M., Bourdon, B., Nimmo, F., Mezger, K., Palme, H., Jacobsen, S.B., Yin, Q.-Z., Halliday, A.N., 2009. Hf–W chronology of the accretion and early evolution of asteroids and terrestrial planets. Geochim. Cosmochim. Acta 73, 5150–5188.
Kleine, T., Hans, U., Irving, A.J., Bourdon, B., 2012. Chronology of the angrite parent body and implications for core formation in protoplanets. Geochim. Cosmochim. Acta 84, 186–203.
Krein, S.B., Behn, M.D., Grove, T.L., 2020. Origins of Major Element, Trace Element, and Isotope Garnet Signatures in Mid-Ocean Ridge Basalts. *Journal of Geophysical Research: Solid*. Earth 125.
Kress, V.C., Carmichael, I.S.E., 1991. The compressibility of silicate liquids containing Fe2O3 and the effect of composition, temperature, oxygen fugacity and pressure on their redox states. Contrib. Miner. Petrol. 108, 82–92.
Kurat, G., Varela, M.E., Brandstätter, F., Weckwerth, G., Clayton, R.N., Weber, H.W., Schultz, L., Wäsch, E., Nazarov, M.A., 2004. D'Orbigny: A non-igneous angritic achondrite? Geochim. Cosmochim. Acta 68, 1901–1921.
Liebske, C., Khan, A., 2019. On the principal building blocks of Mars and Earth. Icarus 322, 121–134.
Lodders, K., 2003. Solar System Abundances and Condensation Temperatures of the Elements. Astrophys J 591, 1220–1247.
Lofgren, G.E., Lanier, A.B., 1992. Dynamic crystallization experiments on the Angra dos Reis achondritic meteorite. Earth Planet. Sci. Lett. 111, 455–466.
Longhi, J., 1999. Phase equilibrium constraints on angrite petrogenesis. Geochim. Cosmochim. Acta 63, 573–585.
Markowski, A., Quitte, G., Kleine, T., Halliday, A., Bizzarro, M., Irving, A., 2007. Hafnium–tungsten chronometry of angrites and the earliest evolution of planetary objects. Earth Planet. Sci. Lett. 262, 214–229.

McCord, T.B., Adams, J.B., Johnson, T.V., 1970. Asteroid Vesta: Spectral Reflectivity and Compositional Implications. Science 168, 1445–1447.
Mccoy, T., Ketcham, R., Wilson, L., Benedix, G., Wadhwa, M., Davis, A., 2006. Formation of vesicles in asteroidal basaltic meteorites. Earth Planet. Sci. Lett. 246, 102–108.
McKay, G., Le, L., Wagstaff, J., Lindstrom, D., 1988a. Experimental Trace Element Partitioning for LEW 86010: Petrogenesis of a Unique Achondrite. Meteoritics 23, 289.
McKay, G., Lindstrom, D., Le, L., Yang, S.-R., 1988b. Experimental studies of synthetic LEW 86010 analogs: Petrogenesis of a unique achondrite. In *Lunar and Planetary Science Conference*, 760–761.
McKay, G., Lindstrom, D., Yang, S.-R., Wagstaff, J., 1988c. Petrology of Unique Achondrite Lewis Cliff 86010. In *Lunar and Planetary Science Conference*, 762–763.
McKay, G., Crozaz, G., Wagstaff, I., Yang, S.R., Lundberg, L., 1990. A Petrographic, Electron Microprobe, Study of Mini-Angrite Lewis Cliff 87051. In *Lunar and Planetary Science Conference*, 771–772.
McKay, G., Le, L., Wagstaff, J., Crozaz, G., 1994. Experimental Partitioning of Rare-Earth Elements and Strontium - Constraints on Petrogenesis and Redox Conditions during Crystallization of Antarctic Angrite Lewis Cliff-86010. Geochim. Cosmochim. Acta 58, 2911–2919.
McKibbin, S.J., O'Neill, H.S.C., 2018. Petrogenesis of D'Orbigny-like angrite meteorites and the role of spinel in the angrite source. Meteorit. Planet. Sci. 53, 306–325.
Médard, E., Grove, T.L., 2008. The effect of H_2O on the olivine liquidus of basaltic melts: experiments and thermodynamic models. Contrib. Miner. Petrol. 155, 417–432.
Médard, E., McCammon, C.A., Barr, J.A., Grove, T.L., 2008. Oxygen fugacity, temperature reproducibility, and H_2O contents of nominally anhydrous piston-cylinder experiments using graphite capsules. Am. Mineral. 93, 1838–1844.
Mikouchi, T., Miyamoto, M., McKay, G., Le, L., 2001. Cooling Rate Estimates of Quenched Angrites: Approaches by Crystallization Experiments and Cooling Rate Calculations of Olivine Xenocrys. In *Annual Meteoritical Society Meeting*, p. A134.
Mikouchi, T., McKay, G., Le, L., Mittlefehldt, D.W., 2000. Preliminary Examination of Sahara 99555: Mineralogy and Experimental Studies of a New Angrite. In: In *Lunar and Planetary Science Conference*, p. 1970.
Mikouchi, T., McKay, G.A., Jones, J.H., 2004. Sahara 99555 and D'Orbigny: Possible Pristine Parent Magma of Quenched Angrites. In: In *Lunar and Planetary Science Conference*, p. 1504.
Mittlefehldt, D.W., Killgore, M., Lee, M.T., 2002. Petrology and geochemistry of D'Orbigny, geochemistry of Sahara 99555, and the origin of angrites. Meteorit. Planet. Sci. 37, 345–369.
Mittlefehldt, D.W., Lindstrom, M.M., 1990. Geochemistry and Genesis of the Angrites. Geochim. Cosmochim. Acta 54, 3209–3218.
Morbidelli, A., Libourel, G., Palme, H., Jacobson, S.A., Rubie, D.C., 2020. Subsolar Al/Si and Mg/Si ratios of non-carbonaceous chondrites reveal planetesimal formation during early condensation in the protoplanetary disk. Earth Planet. Sci. Lett. 538, 116220.
Nakashima, D., Nagao, K., Irving, A.J., 2018. Noble gases in angrites Northwest Africa 1296, 2999/4931, 4590, and 4801: Evolution history inferred from noble gas signatures. Meteorit. Planet. Sci. 53, 952–972.
O'Neill, H.S., 1987. Quartz-fayalite-iron and quartz-fayalite-magnetite equilibria and the free energy of formation of fayalite (Fe_2SiO_4) and magnetite (Fe_3O_4). Am. Mineral. 72, 67–75.
O'Neill, H.St.C., Pownceby, M.I., 1993. Thermodynamic data from redox reactions at high temperatures. I. An experimental and theoretical assessment of the electrochemical method using stabilized zirconia electrolytes, with revised values for the Fe-FeO, Co-CoO, Ni-NiO and Cu-Cu2O oxygen buffers, and new data for the W-WO2 buffer. Contrib. Miner. Petrol. 114, 296–314.
Obata, M., 1976. The solubility of Al_2O_3 in orthopyroxenes in spinel and plagioclase peridotites and spinel pyroxenite. Am. Mineral. 61, 804–816.
Papike, J.J., Burger, P.V., Bell, A.S., Shearer, C.K., 2017. Mn-Fe systematics in major planetary body reservoirs in the solar system and the positioning of the Angrite Parent Body: A crystal-chemical perspective. Am. Mineral. 102, 1759–1762.
Premo, W.R., Tatsumoto, M., 1995. Pb isotopic systematics of angrite Asuka 881371. Twentieth Symposium on Antarctic Meteorites, In Antarctic Meteorites XX, pp. 204–206.
Prinz, M., Weisberg, M.K., Nehru, C.E., 1988. LEW 86010, A Second Angrite: Relationship to CAI's and Opaque Matrix. In: In *Lunar and Planetary Science Conference*, pp. 949–950.
Riches, A.J.V., Day, J.M.D., Walker, R.J., Simonetti, A., Liu, Y., Neal, C.R., Taylor, L.A., 2012. Rhenium–osmium isotope and highly-siderophile-element abundance systematics of angrite meteorites. Earth Planet. Sci. Lett. 353–354, 208–218.
Righter, K., 2008. Siderophile element depletion in the angrite parent body (APB) mantle: due to core formation? In *Lunar and Planetary Science Conference*, p. 1936.
Rivkin, A.S., Trilling, D.E., Thomas, C.A., DeMeo, F., Spahr, T.B., Binzel, R.P., 2007. Composition of the L5 Mars Trojans: Neighbors, not siblings. Icarus 192, 434–441.
Rivoldini, A., Van Hoolst, T., Verhoeven, O., 2009. The interior structure of Mercury and its core sulfur content. Icarus 201, 12–30.
Ruzicka, A., Snyder, G.A., Taylor, L.A., 1997. Vesta as the howardite, eucrite and diogenite parent body: Implications for the size of a core and for large-scale differentiation. Meteorit. Planet. Sci. 32, 825–840.
Ruzicka, A., Floss, C., Hutson, M., 2012. Amoeboid olivine aggregates (AOAs) in the Efremovka, Leoville and Vigarano (CV3) chondrites: A record of condensate evolution in the solar nebula. Geochim. Cosmochim. Acta 79, 79–105.
Sanborn, M.E., 2012. The Petrogenesis of Angrites and Martian Meteorites Inferred from Isotope and Trace Element Systematics. Arizona State University.
Sanborn, M., Wadhwa, M., 2010. Rare earth element geochemistry of quenched angrites Northwest Africa 1296 and Northwest Africa 1670. In: In *Lunar and Planetary Science Conference*, p. 1490.
Sanborn, M.E., Wadhwa, M., 2021. Trace element geochemistry of coarse-grained angrites from Northwest Africa: Implications for their petrogenesis on the angrite parent body. Meteorit. Planet. Sci. 56, 482–499.
Santos, A.R., Agee, C.B., Shearer, C.K., McCubbin, F.M., 2016. Northwest Africa 8535 and Northwest Africa 10463: new insights into the angrite parent body. In: In *Lunar and Planetary Science Conference*, p. 2590.
Sarafian, A.R., Hauri, E.H., McCubbin, F.M., Lapen, T.J., Berger, E.L., Nielsen, S.G., Marschall, H.R., Gaetani, G.A., Righter, K., Sarafian, E., 2017a. Early accretion of water and volatile elements to the inner Solar System: evidence from angrites. Phil. Trans. R. Soc. A. 375, 20160209.
Sarafian, A.R., Nielsen, S.G., Marschall, H.R., Gaetani, G.A., Hauri, E.H., Righter, K., Sarafian, E., 2017b. Angrite meteorites record the onset and flux of water to the inner solar system. Geochim. Cosmochim. Acta 212, 156–166.
Scott, E.R.D., Bottke, W.F., 2011. Impact histories of angrites, eucrites, and their parent bodies. Meteorit. Planet. Sci. 46, 1878–1887.
Shearer, C.K., Bell, A.S., Burger, P.V., Papike, J.J., Jones, J., Le, L., 2016. The Cr redox record of fO_2 variation in angrites. Evidence for redox conditions of angrite petrogenesis and parent body. In: In *Lunar and Planetary Science Conference*, p. 1903.
Shi, P., 1992. Basalt evolution at low pressure: implications from an experimental study in the system CaO-FeO-MgO-Al_2O_3-SiO_2. Contrib. Miner. Petrol. 110, 139–153.
Shirai, N., Humayun, M., Irving, A.J., 2009a. The bulk composition of coarse-grained meteorites from laser ablation analysis of their fusion crusts. In: In *Lunar and Planetary Science Conference*, p. 2170.
Shirai, N., Humayun, M., Righter, K., 2009b. Analysis of moderately siderophile elements in angrites: implications for core formation of the angrite parent body. In: In *40th Lunar Planetary Science Conference*, p. 2122.
Spandler, C., O'Neill, H.S.C., 2010. Diffusion and partition coefficients of minor and trace elements in San Carlos olivine at 1,300°C with some geochemical implications. Contrib. Miner. Petrol. 159, 791–818.
Steenstra, E.S., Sitabi, A.B., Lin, Y.H., Rai, N., Knibbe, J.S., Berndt, J., Matveev, S., van Westrenen, W., 2017. The effect of melt composition on metal-silicate partitioning of siderophile elements and constraints on core formation in the angrite parent body. Geochim. Cosmochim. Acta 212, 62–83.
Till, C.B., Grove, T.L., Krawczynski, M.J., 2012. A melting model for variably depleted and enriched lherzolite in the plagioclase and spinel stability fields: a model for melting modified mantle. J. Geophys. Res., 117
Tissot, F.L.H., Dauphas, N., Grove, T.L., 2017. Distinct $^{238}U/^{235}U$ ratios and REE patterns in plutonic and volcanic angrites: Geochronologic implications and evidence for U isotope fractionation during magmatic processes. Geochim. Cosmochim. Acta 213, 593–617.
Toplis, M.J., 2005. The thermodynamics of iron and magnesium partitioning between olivine and liquid: criteria for assessing and predicting equilibrium in natural and experimental systems. Contrib. Miner. Petrol. 149, 22–39.
Tormey, D.R., Grove, T.L., Bryan, W.B., 1987. Experimental petrology of normal MORB near the Kane Fracture Zone: 22°-25° N, mid-Atlantic ridge. Contrib. Miner. Petrol. 96, 121–139.
Varela, M.E., Kurat, G., Zinner, E., Métrich, N., Brandstätter, F., Ntaflos, T., Sylvester, P., 2003. Glasses in the D'Orbigny angrite. Geochim. Cosmochim. Acta 67, 5027–5046.
Varela, M.E., Kurat, G., Zinner, E., Hoppe, P., Ntaflos, T., Nazarov, M.A., 2005. The non-igneous genesis of angrites: Support from trace element distribution between phases in D'Orbigny. Meteorit. Planet. Sci. 40, 409–430.
Varela, M.E., Hwang, S.-L., Shen, P., Chu, H.-T., Yui, T.-F., Iizuka, Y., Brandstätter, F., Abdu, Y.A., 2017. Olivinites in the angrite D'Orbigny: Vestiges of pristine reducing conditions during angrite formation. Geochim. Cosmochim. Acta 217, 349–364.
Wang, H., Weiss, B.P., Bai, X.-N., Downey, B.G., Jun, W., Jiajun, W., Suavet, C., Fu, R.R., Zucolotto, M.E., 2017. Lifetime of the solar nebula constrained by meteorite paleomagnetism. Science 355, 623–627.
Warren, P.H., 2011. Stable-isotopic anomalies and the accretionary assemblage of the Earth and Mars: A subordinate role for carbonaceous chondrites. Earth Planet. Sci. Lett. 311, 93–100.
Warren, P.H., Kallemeyn, G.W., 1990. Geochemistry of the LEW87051 Angrite and Other Basaltic Achondrites. In: In *Lunar and Planetary Science Conference*, p. 1295.
Weiss, B.P., Berdahl, J.S., Elkins-Tanton, L., Stanley, S., Lima, E.A., Carporzen, L., 2008. Magnetism on the Angrite Parent Body and the Early Differentiation of Planetesimals. Science 322, 713–716.
Wilson, L., Keil, K., 1991. Consequences of explosive eruptions on small Solar System bodies: the case of the missing basalts on the aubrite parent body. Earth Planet. Sci. Lett. 104, 505–512.
Wyllie, P.J., Donaldson, C.H., Irving, A.J., Kesson, S.E., Merrill, R.B., Presnall, D.C., Stolper, E.M., Usselman, T.M., Walker, D., 1981. Experimental petrology of basalts and their source rocks. In Experimental petrology of basalts and their source rocks Pergamon Press, New York, pp. 493–630.

Yanai, K., 1994. Angrite Asuka-881371: Preliminary examination of a unique meteorite in the Japanese collection of Antarctic meteorites. Antarct. Meteor. Res. 7, 30.

Yang, H.-J., Kinzler, R.J., Grove, T.L., 1996. Experiments and models of anhydrous, basaltic olivine-plagioclase-augite saturated melts from 0.001 to 10 kbar. Contrib. Miner. Petrol. 124, 1–18.

Zhu, K., Moynier, F., Wielandt, D., Larsen, K.K., Barrat, J.-A., Bizzarro, M., 2019. Timing and Origin of the Angrite Parent Body Inferred from Cr Isotopes. Astrophys. J. Lett. 877, L13.